ELECTRONIC GROUND STATE PROPERTIES OF COULOMB BLOCKADED QUANTUM DOTS

A DISSERTATION

SUBMITTED TO THE DEPARTMENT OF PHYSICS

AND THE COMMITTEE ON GRADUATE STUDIES

OF STANFORD UNIVERSITY

IN PARTIAL FULFILLMENT OF THE REQUIREMENTS

FOR THE DEGREE OF

DOCTOR OF PHILOSOPHY

Satyadev Rajesh Patel

June 2002

I certify that I have read this dissertation and that in my opinion it is fully adequate, in scope and quality, as a dissertation for the degree of Doctor of Philosophy.

Charles M. Marcus
(Principal Adviser)

I certify that I have read this dissertation and that in my opinion it is fully adequate, in scope and quality, as a dissertation for the degree of Doctor of Philosophy.

Alexander Fetter

I certify that I have read this dissertation and that in my opinion it is fully adequate, in scope and quality, as a dissertation for the degree of Doctor of Philosophy.

James S. Harris, Jr.

I certify that I have read this dissertation and that in my opinion it is fully adequate, in scope and quality, as a dissertation for the degree of Doctor of Philosophy.

Yoshihisa Yamamoto

Approved for the University Committee on Graduate Studies:

Abstract

Conductance through quantum dots at low temperature exhibits random but repeatable fluctuations arising from quantum interference of electrons. The observed fluctuations follow universal statistics arising from the underlying universality of quantum chaos. Random matrix theory (RMT) has provided an accurate description of the observed universal conductance fluctuations (UCF) in "open" quantum dots (device conductance $\geq e^2/h$). The focus of this thesis is to search for and decipher the underlying origin of similar universal properties in "closed" quantum dots (device conductance $\leq e^2/h$). A series of experiments is presented on electronic ground state properties measured via conductance measurements in Coulomb blockaded quantum dots. The statistics of Coulomb blockade (CB) peak heights with zero and non-zero magnetic field measured in various devices agree qualitatively with predictions from Random Matrix Theory (RMT). The standard deviation of the peak height fluctuations for non-zero magnetic field is lower than predicted by RMT; the temperature dependence of the standard deviation of the peak height for non-zero magnetic field is also measured. The second experiment summarizes the statistics of CB peak spacings. The peak spacing distribution width is observed to be on the order of the single particle level spacing, Δ, for both zero and non-zero magnetic field. The ratio of the zero field peak spacing distribution width to the non-zero field peak spacing distribution width is ~ 1.2; this is good agreement with predictions from spin-resolved RMT predictions. The standard deviation of the non-zero magnetic field peak spacing distribution width shows a $T^{-1/2}$ dependence in agreement with a thermal averaging model. The final experiment summarizes the measurement of the peak height correlation length versus temperature for various quantum dots. The peak height correlation length versus temperature saturates in small quantum dots, suggesting spectral scrambling after adding a small number of electrons. Larger devices show saturation to a higher value suggesting that the larger devices are less prone to spectral scrambling. Enhanced correlation, arising possibly from pairs of CB peaks with similar peak heights, is observed in all dots at low temperature.

Acknowledgements

As I am writing this thesis, it has been over four years since I finished my last experiment in the lab. Given this fact, I am very thankful for my memory and good notes taken in my lab notebooks. I wanted to finish my thesis earlier, but there were always some fires to extinguish at Reflectivity or in my personal life. However, it is now finally time to finish up my thesis and bring closure to my life as a graduate student.

I would like to begin the acknowledgements by thanking Charles Marcus, my adviser. I would have never become an experimental scientist were it not for his guidance, patience, and enthusiasm. He has provided tremendous input into the direction of this research; his involvement in the theoretical community has allowed me to get assistance from the best experts in the field during my attempts to understand the implications of my experimental data. I thank Alexander Fetter for working with me as a 1st year graduate student; it was because of him that I was able to get a glimpse of theoretical research in physics. I also want to thank him for the career guidance that he offered me towards the end of my research work and for being on my reading committee. I thank James Harris, Jr. for supplying the 2-dimensional electron gas (2DEG) used for a large fraction of my experiments. Most of the measurements, sensitive to switching noise in the 2DEG, were only possible because of the high quality of material grown by his group at Stanford. I also thank him for being in my reading committee. Finally, I thank Yoshihisa Yamamoto for his help in setting up Ginzton laboratories at Stanford; he was instrumental in purchasing and setting up the Leica SEM in the lab. All of the fabrication process work for my samples was done in Ginzton using the SEM. I also want to thank him for being on my reading committee.

In Charlie's lab, I want to begin by thanking my good friends and co-graduate students: Andy Huibers, Sara Cronenwett and Josh Folk. I learned everything I know about quantum dot fabrication from Andy; Andy's easy going nature and support kept me from going mad during my time as a graduate student. Andy is by far one of the most creative people I have ever met; he is one of the main reasons I have never regretted my decision to join Reflectivity after my work at Stanford. Over many experiments, Sara was the best collaborator I could have had; her enthusiasm helped drive me when I had none of my own. Sara is a dear friend, and I wish her

well in her future endeavors. Josh was the 1st person to expose me to transport measurements in the CB regime; he also helped me learn the ropes on operating the dilution refrigerator. Josh's drive to do exceptional experimental work set the standard for my own work in the lab. I am sure that Josh will find success and happiness wherever he goes in the future. I also thank other students in Charlie's lab for their friendship and support: Duncan Stewart, Michael Switkes, David Sprinzak, Sebastian Maurer, Sandra Godijn, Randall True, Fred Mancoff, Lukasz Zelinski, Rob ver der Hage, Kevin Birnbaum, John Stockton, and Steve Grossman.

I thank my collaborators not acknowledged already: Mehmet Gokcedag, Yoram Alhassid, Doug Stone, Art Gossard, Ken Campman and Cem Duruoz. I am also grateful for the help provided by Tom Carven in the Gintzon clean room over many months of device fabrication time.

I realize now that I have followed a path that was exposed to me by two of my teachers in high school. I thank T. Scott Dukes (physics teacher, Newport Harbor High School) for introducing me to physics and Arthur Wayman (mathematics professor, Orange Coast College/California State University Long Beach) for introducing me to subtleties of mathematics. My love for mathematics and sciences is a direct result of the teachings of these two men. When I return to teaching (in the near future), I only hope that I will be able to teach my students with the same passion with which they have taught me.

Lastly, I thank my friends (not mentioned already) for their support during my graduate school work: Tejas, Gaurang, Raj, Dhru, Harini, Arti, Ray, Joe, Charles, Jon, Kavita, Mamta, Priya, Reed, Ritu, Vikas and Cindy. I extend thanks to my friends and co-workers at Reflectivity. I thank my family for their love and support: Anupama, Mamta, Ketan, Raju, Apeksha, Sayani, Prabhu, Jyotsna, Bharati and Viresh. I would particularly like to thank my parents, Rajesh and Priti, for having more faith in me than I did in myself when I was younger. They have helped me become a better person through their sacrifices over the past 30 years. Finally, I would like to thank my wife, Kaveri, for putting up with me and providing infinite love and friendship over the past 8 years.

Contents

List of Tables

List of Figures

Chapter 1

Introduction

1.1 Introduction and Motivation

Quantum dots provide an experimental system to probe our understanding of single-particle and many-particle physics. One of the main efforts currently under task is the study of the applicability of a single-particle model to a many-particle system. The Coulomb blockade (CB) regime in transport through quantum dots provides a near perfect system to probe the applicability of the single particle model to a system involving many electrons[1]. Particularly, the CB regime is characterized by a large charging energy, E_C, which suppresses transport through the device except at points of degeneracy in dot occupation number. This charging energy represents the interaction energy of the electrons on the dot; hence, E_C represents a characteristic energy of the many-particle system. Coulomb blockade in isolated quantum dots at low temperatures is characterized by transport through a single level of the dot spectrum[2]. As such, the measured transport properties provide statistics of a single level on the background of a many-particle interacting system.

In open systems, measured transport properties exhibit mesoscopic fluctuations (random but repeatable fluctuations arising from quantum interference)[3-8]. The statistics of the mesoscopic fluctuations exhibit universal features which are due to the underlying universalities of quantum chaos[9-12]. Random Matrix Theory (RMT) provides one of the theoretical frameworks for understanding and predicting transport properties in open systems[13, 14]. RMT also provides a prediction of the universal statistics of conductance amplitudes and level spacings

within the CB regime. The underlying assumption of RMT is that the (non-interacting) single-particle model is an adequate description of the level spectrum and couplings of the quantum dot. Deviations from the predicted statistics would, hence, suggest either a many-particle effect or an effect not included in the RMT formulation.

This thesis summarizes measurements of the conductance and level spacing statistics in the CB regime over many devices. The measurements are restricted to CB transport through the ground state of the dot; transport through excited states of a quantum dot in the CB regime have been studied in other experiments[15, 16]. The goal of the thesis is examine transport properties for underlying universalities. Additionally, a secondary goal is to determine a theoretical frame work which provides plausible explanations for measured data.

1.2 Organization of this Thesis

This chapter provides an introduction to and some motivation for the study of statistics of transport properties in the CB regime.

Chapter 2 gives an introduction to quantum dots, summarizes the measurement set-up used in the experiments, describes CB phenomena and discusses the techniques used to extract the device energy scales, and provides a list of device parameters for the dots measured. Chapter 3 describes the results of the experiments to measure CB peak height statistics. Chapter 4 discusses CB peak spacing statistics. Chapter 5 summarizes a measurement of the level spectrum sensitivity to the addition of electrons in quantum dots of different sizes. The results are summarized in Chapter 6. Appendix A summarizes the device fabrication procedure. Appendix B summarizes techniques to reduce device noise during measurement. Appendix C shows the circuit diagram used to combine ac and dc bias for the measurement of Δ in Section 2.4.3.

In all chapters and appendices, the figures and tables are placed at the end in order to not interrupt the flow of the text.

Chapter 2

Coulomb Blockade in Quantum Dots

2.1 Introduction

Quantum dots have been used extensively to investigate electron transport in open (greater than or equal to one conducting channel into and out of the quantum dot) and closed systems[17-19]. A laterally defined cavity in a 2-dimension electron gas (2DEG) is one particular example of a quantum dot. This work makes use of these types of devices to further investigate transport properties in closed systems. The sections in this chapter describe the quantum dot design, the measurement set-up and the transport behavior in the CB regime.

2.2 GaAs/AlGaAs 2DEG Devices

The quantum dots studied in this thesis are made in a two-dimensional electron gas (2DEG) which forms at the interface of a GaAs/$Al_xGa_{1-x}As$ heterostructure grown by molecular-beam-epitaxy[20]. The heterostructure, seen in Fig. 2-1, is grown on an epitaxially grown GaAs layer formed on top of a bare GaAs substrate; a layer of 50 to 200 nm thick layer of AlGaAs is grown epitaxially to form the interface for the 2DEG. A layer of thin (~ 10 nm) GaAs cap is grown on the top of the AlGaAs to prevent oxidation. The AlGaAs layer provides free electrons to the 2DEG from a region of n-type dopants. The band diagram of the heterostructure forms a well at the GaAs/AlGaAs interface; at low temperatures, only the lowest level of the sub-band falls below the Fermi energy. As such, the electrons are confined to a region in the 2-dimensional

plane within ~ 10 nm of the interface. The typical Fermi energy of the 2DEG is ~ 10 meV; this is much lower than energy difference between the lowest sub-band and next available sub-band (~ 150 eV). The temperatures used in the experiments are less than 1 K (~ 86 μeV); the voltage biases used for conductance measurements are < 100 μV (typically ~ 5 μV). The only slight mismatch between the GaAs and AlGaAs lattices produces a low number of interfacial defects. Additionally, the n-type dopants in the AlGaAs layer are located 20 – 40 nm from the interface to minimize the effect of scattering from charged impurities at the 2DEG. These two heterostructure properties lead to a 2DEG with a mean free path of 10's of microns. Typical values for the parameters of a 2DEG formed in a GaAs/AlGaAs heterostructure are given in Table 2-1.

To form the quantum dot, the 2DEG is laterally shaped to form a cavity with the use of surface gates (see Fig. 2-2). These gates, in contrast to the NiAuGe contacts (described below), do not make electrical contact to the 2DEG. Applying a negative bias on the surface gates with respect to the 2DEG forces the electrons under the gates to be depleted. Selectively depleting regions of the 2DEG (by patterning surface gates) permits the definition of the quantum dot.

One of the major advancements made during the experiments in this thesis was the design of quantum dots with many independently controllable gates. The multi-gate designs permit the accurate tuning of the dot point contacts (tunnel barriers) with the source and drain regions of the 2DEG. The multi-gate design also allows the shape of the quantum dot to be changed without affecting the conductance into and out of the quantum dot.

Electrical contact is made to the 2DEG through annealed NiAuGe contacts on the surface of the heterostructure (see Fig. 2-1); these contacts are tested to verify "ohmic" behavior. Transport through the dot is measured by applying a fixed current through the dot or by applying a fixed voltage bias across the device.

2.3 Measurement Set-up

The resistance of the device in the CB regime is sufficiently large compared to the ohmic contact resistance and the lead resistance that a 2-wire, voltage bias measurement can be used to measure conductance. A current bias measurement is not possible in the CB regime as the device resistance grows to a large value between the CB peaks (in the blockade state); the large resistance in the blockade state would drive the voltage across the device into a regime out of the linear, single-level transport regime. The sum of the ohmic contact and lead resistance is < 1 kΩ,

and the device resistance is typically on the order of 100,000 kΩ. This permits an accurate measurement of the device conductance from the measured current in the voltage bias mode.

A typical voltage bias measurement set-up is shown in Fig. 2a. A fixed voltage bias from a lock-in is applied to the source side of the device; the drain is connected to an Ithaco 1211 current pre-amp. The output of the pre-amp is feed back into the lock-in for a current measurement. Two 50 Ω resistors are placed in series on the lock-in high and low outputs to prevent the lock-in shield (low) from floating by a few μVs. The gates are biased negative with respect to the drain using a battery box in addition to a computer controlled voltage supply board. In the measurement, it is important to keep the applied bias below the temperature, the single particle level spacing Δ and charging energy E_C of the device, $eV_{bias} < kT$, Δ, E_C; these sets of inequalities ensure that the transport on a CB occurs only through a single level of the quantum dot. The formulation of these requirements is provided in the next section.

This 2-wire measurement set-up is modified slightly in order to make a direct measurement of Δ; the modification includes a direct measurement of the ac and dc components of the applied bias as shown in Fig. 2-3b. The dc bias is added to the ac bias from the lock-in using an "adder box" built by D. Stewart; the adder box acts like a 1,000:1 divider for the ac signal and a 100,000:1 divider for the dc signal at 13 Hz. Details of the adder box can be found in Appendix C[21]. The ac component of the applied bias is measured directly using a phase locked lock-in; the dc component of the bias is measured using a DMM after amplifying the signal using a SRS560 voltage pre-amp. This measurement set-up allows a direct measurement of the applied bias at the dot; particularly, it can be used to see if the 50 Ω resistors in series mentioned above remedy the floating of the lock-in shield.

2.4 Coulomb Blockade in Quantum Dots

2.4.1 Coulomb Blockade Theory

Coulomb blockade is observed in a quantum dot when the total conductance through the device is below e^2/h = 1/25813 Ω; particularly, the conductance of each point contact (leads into and out of the quantum dot) is less than $2e^2/h$. In this regime, the transport of electrons occurs via tunneling into and out of the quantum dot. In the CB regime, the quantum dot can be conceptualized simply as a metal island coupled capacitively to the source, the drain and a gate as depicted in Fig. 2-4; in this picture, tunneling is permitted into and out of the quantum dot from

the source and drain (via the resistive element) but not from the gate[2, 20]. Classically, the charge on the quantum dot is continuous, linear with the voltage across the dot. In actuality, the charge on the dot is quantized to an integral number of electrons. The charge state of the quantum dot can be depicted as shown in Fig. 2-5. The charge imbalance between the quantum dot and the source/drain, see Fig. 2-5a, oscillates between $e/2$ and $-e/2$ as the voltage of the dot is tuned by changing the gate voltage. The dot occupancy increases with the dot voltage in the form of a staircase as shown in Fig. 2-5b; conductance through the dot is only possible at points of degeneracy where the charge on the quantum dot can change between N and $N+1$[22]. All of the CB measurements in this thesis are restricted to the regime where the transport occurs via the ground state of the N or $N+1$ electron system; for larger applied bias, transport becomes possible through both the ground and excited states of the system. This large-bias regime of transport has been studied by many experimentalists[15, 16, 23-28]; the techniques used in those experiments are used to make a measurement of the quantum level spacing of the dot as discussed in section 2.4.3. The conductance is shown in Fig. 2-5c as a function of dot voltage; periodic CB peaks appear when the electron occupancy of the quantum dot is allowed to change by one. The spacing of adjacent CB peaks provides a measure of the charging energy (neglecting the contribution from single particle energy levels within the dot); this relationship is derived in Section 2.4.4. In the blockade regime (between adjacent peaks), the quantum dot occupancy is an integral number of electrons. This picture is accurate as long as the charging energy (energy required to change the dot occupancy by 1) is larger than the temperature of the dot and the applied bias.

The experiments in this thesis focus on CB transport in the regime of low temperatures with near zero intrinsic level broadening. The energy level diagram for the dot with respect to the source/drain can be depicted as shown in Fig. 2-6. The levels in the quantum dots are broadened (due to coupling between the dot and the source/drain) by ~ 0.5 μeV; this target is achieved by increasing the tunneling barriers into and out of the quantum dot by tuning the point contact surface gates. The applied bias is selected to be less than the base temperature of the device; this assures that the Fermi levels at the source and the drain are offset relative to each other by less than the temperature broadening of the Fermi surface. The lowest base temperature for the experiments is ~ 50 mK (corresponding to 4.3 μeV); the differential conductance is measured with an ac voltage bias in the range of 2 – 5 μV. The single particle level spacing is derived from the 2d density of states; the level spacing, Δ, is typically 10 – 40 μeV assuming non-spin

degenerate levels within the quantum dot. Finally, the charging energy E_C of the quantum dot is ~ 500 – 1000 μeV.

Transport properties (conductance line-shapes and their temperature dependence) in the regime Γ (level broadening) < kT, $\Delta < E_C$ have been studied theoretically by Beenakker[2]. In the near-zero applied bias transport regime, the conductance process is described by resonant tunneling. The conductance line-shape in the regime $\Gamma < kT < \Delta < E_C$ is given by:

$$g = \frac{e^2}{h}\frac{\pi}{2kT}\frac{\Gamma_l\Gamma_r}{\Gamma_l+\Gamma_r}\cosh^{-2}\left(\frac{E_0-\eta eV_g}{2kT}\right) \qquad [2.1]$$

where V_g is the applied gate voltage, Γ_l, Γ_r are the source-dot and dot-drain tunneling rates multiplied by $\hbar$ (define $\Gamma = (\Gamma_l + \Gamma_r)$), E_0 is the resonant level energy and η is the ratio of the gate capacitance to total dot capacitance. Within this regime, transport occurs via a single level of the quantum dot. The expressions for Γ_l, Γ_r include the overlap between the source/drain wave-function and the wave-function of the level contributing to transport. At temperatures larger than Δ ($\Gamma < \Delta < kT < E_C$), transport occurs via all quantum levels within the temperature smeared Fermi surface energy window; here the line-shape is given by:

$$g = \frac{e^2}{h}\frac{1}{2kT}\frac{1}{4\Delta}\frac{\Gamma_l\Gamma_r}{\Gamma_l+\Gamma_r}\cosh^{-2}\left(\frac{E_0-\eta eV_g}{2.5kT}\right) \qquad [2.2]$$

The Beenakker formulation presented here sets the model under which the experimental data is interpreted to extract properties of the CB peak height, CB peak spacing and CB spectral scrambling statistics[2]. All data presented in the thesis is taken with symmetric coupling between the source-dot and dot-drain, i.e. $\langle\Gamma_l\rangle = \langle\Gamma_r\rangle$; for a given dot configuration, the value of $\langle\Gamma_l\rangle$, $\langle\Gamma_r\rangle$ can be calculated from $\langle g\rangle$ (in the configuration at $kT < \Delta$) and Eq. 2.1.

Outside of the work presented in this thesis, there is considerable experimental and theoretical investigation into other CB transport phenomena. Particularly, there has been extensive theoretical and experimental work on transport properties in the partially blockaded region (non-zero conductance between adjacent CB peaks)[29, 30]. Experimental investigation into the level spectrum of a quantum dot in the CB regime has been carried out on lateral and vertical quantum dots[15, 16, 28]. Finally, there has been work studying CB phenomena in a quantum dot with one conducting channel[31].

2.4.2 Measurement of Device Temperature

Device temperature measurement is made possible by measuring the width of the CB peak versus temperature. The peak FWHM (full width at half maximum) scales as $3.53kT$ for temperatures $kT < \Delta$; the FWHM remains linear in temperature with a different slope ($4.35kT$) for temperatures $\Delta < kT$[32]. Data in Fig. 2-7 shows the measured FWHM versus the dilution fridge temperature (measured by a Ruthenium Oxide resistor). A transition from the low temperature slope to the high temperature slope occurs around 800 mK. There is observable decoupling of the device temperature from the fridge temperature due to heat influx from the measurement leads into the quantum dot.

In order to lower the device temperature, improvements were made to the thermal sinking and RC filtering of the device leads. The details on the improvement are provided in appendix C of A. Huibers' thesis[33]. The FWHM temperature dependence is shown in Fig. 2-8 for another quantum dot after the improvements. At the base temperature of the fridge, the device temperature is lowered to ~ 45 mK after the wiring changes.

The FWHM dependence on temperature also provides a means of measuring the gate to dot capacitance ratio η based on the relationship $e\eta\mathrm{FWHM} = 3.53kT$ at low temperatures. Using this relationship, the calculated value of η is 0.0583 (0.0651) for the data shown in Fig. 2-7 (Fig. 2-8). The measured value of η is used to convert other measurements in gate voltage to energy differences within the quantum dot.

2.4.3 Measurement of Δ, Single Particle Level Spacing

The theoretical calculation of the single particle level spacing for a quantum dot can be calculated directly from the 2d density of states. Assuming that the energy levels within the dot are spin resolved (i.e. spin symmetry is broken), the single particle level spacing is given by:

$$\Delta = \frac{\partial E}{\partial n} = \frac{\pi\hbar^2}{m^* A} \qquad [2.3]$$

where m^* is the effective mass of the electron and A is the quantum dot area. The assumption of spin resolved levels within the quantum dot is justified based on the absence of even-odd structure in the measured CB peak spacings. This is discussed in Chapter 4 of this thesis.

The single particle level spacing can also be measured directly by applying a dc bias across the quantum dot in the CB regime in addition to the ac bias used to measure the differential

conductance. With an applied dc bias V_{DC} across the dot (with $E_C > V_{DC} > \Delta$), the electrons in the source can tunnel into one of ~ V_{DC}/Δ aligned and un-occupied levels. The levels participating in the transition include both the $N+1$ ground state and any available $N+1$ excited states of the quantum dot. If $V_{DC} = 0$ and $V_{DC} << \Delta$, then the $N+1$ excited states are not available for tunneling since they are (on average) Δ or more above the $N+1$ ground state; this situation is the standard, small bias CB regime. Going back to the finite $E_C > V_{DC} > \Delta$ measurement, the differential conductance shows a peak whenever the $N+1$ ground state or $N+1$ excited state aligns with the source or drain Fermi energy[16]. Hence, a measurement of the differential conductance at finite dc bias provides a measurement of the level spectrum spacing in a quantum dot. An excellent description of transport in this finite dc bias CB regime is presented in Chapter 3 of D. Stewart's thesis[21].

Figure 2-9 shows a typical measurement for Δ using a 200 μV dc bias on top of a 2 μV ac voltage signal. The spacings between the peaks in the conductance at finite bias (Fig. 2-9b) provide measurements of the level spacings between the discrete levels of the quantum dot. The differences in the gate voltage positions of the peaks is converted to energy differences in the quantum dot using η. The average of the 3 spacings measured in this scan reflects an average level spacing of 20 μeV for this device; the calculated Δ from depleted device area is 9 μeV. This observed difference between the measured versus calculated Δ is, as of this writing, unresolved.

2.4.4 Measurement of E_C, Charging Energy

The charging energy E_C is related to the peak spacing between adjacent peaks as the gate voltage V_g is swept. The explicit relationship can be derived assuming a single particle energy model for the dot energy. Figure 2-10 shows two adjacent CB peaks; the peak spacing ΔV_g^N between the $N-1 \leftrightarrow N$ peak and $N \leftrightarrow N+1$ is related to E_C by $e\eta\Delta V_g^N = E_C + s_N$, where s_N is the difference between the $N+1$ and N single particle energies[34].

The derivation of this relationship starts with the CB degeneracy condition:

$$\varepsilon_{N+1} - \varepsilon_N = e\eta V_g^N + \mu, \qquad [2.4]$$

where ε_N is the N-electron ground state energy, V_g^N is the position of the CB peak corresponding to $N \leftrightarrow N+1$ degeneracy and μ is the chemical potential of the dot. The peak spacing ΔV_g^N can be calculated in terms of the ground state energy differences:

$$e\eta\Delta V_g^N = e\eta\left(V_g^N - V_g^{N-1}\right) = \varepsilon_{N+1} - 2\varepsilon_N + \varepsilon_{N-1}. \quad [2.5]$$

Assuming that the N-electron ground state energy can be represented as

$$\varepsilon_N = \sum_{i=1}^{N} \beta_i + \frac{N^2 e^2}{2C_{dot}} \quad [2.6]$$

with i^{th} single particle energies β_i, the above equation simplifies to

$$e\eta\Delta V_g^N = \frac{e^2}{C_{dot}} + \left(\beta_{N+1} - \beta_N\right). \quad [2.7]$$

Here the charging energy E_C is identified as e^2/C_{dot}, and the level spacing is identified as $s_N = \beta_{N+1} - \beta_N$. Since the typical values of E_C are approximately 30 - 50 times the typical values of $\Delta = \langle s_N \rangle_N$ (see Table 2-2), it is customary to express E_C $e\eta\Delta V_g$. The fluctuations of ΔV_g apart from the slowly varying E_C contribution is the subject of Chapter 4; the peak spacing fluctuations are studied to examine the underlying statistics of the single particle level spacing distribution.

2.5 Devices Measured for Thesis Work

A total of seven quantum dots were measured over the course of this thesis work. Table 2-2 summarizes the device parameters for all of the devices.

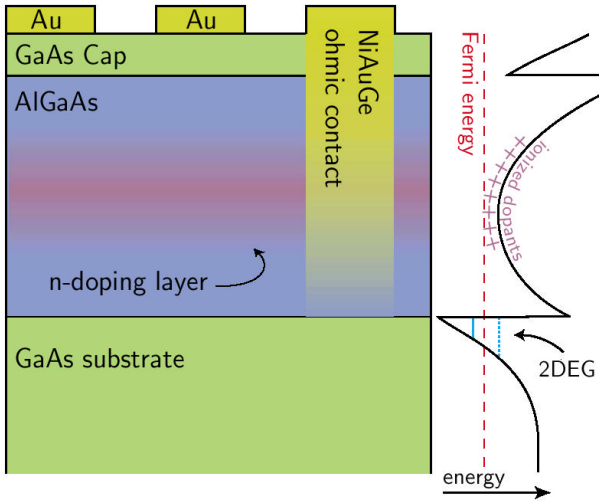

Figure 2-1. GaAs/AlGaAs heterostructure and band diagram. The GaAs/AlGaAs heterostructure is comprised of a bulk GaAs substrate, a layer (~ 50 – 200 nm thick) of $Al_xGa_{1-x}As$, and a plain GaAs cap (~ 10 nm). The AlGaAs layer is partially doped with n-type donors which contribute electrons to a two-dimensional electron gas (2DEG) that forms at the GaAs/AlGaAs interface at low temperature. Gold (Au) gates and NiAuGe ohmic contacts are patterned on the surface during device fabrication. The ohmic contacts are annealed so that their metal diffuses down and makes electrical contact with the 2DEG. The band diagram of the GaAs/AlGaAs wafer is shown on the right with energy on the horizontal axis. At low temperature, electrons fill the triangular potential well at the GaAs/AlGaAs interface up to the Fermi energy, forming the 2DEG. (Figure courtesy of M. Switkes).

2DEG Property	Symbol	Value	Units
Effective mass	m^*	0.067	$m_e = 9.1 \times 10^{-28}$ g
Spin degeneracy	g_s	2	
Valley degeneracy	g_v	1	
Dielectric constant	ε	13.1	$\varepsilon_0 = 8.9 \times 10^{-12}$ Fm^{-1}
Effective Lande g-factor	g^*	–0.44	
Density of states	$\rho(E) = g_s g_v(m^*/2\pi\hbar^2)$	2.8×10^{10}	cm^{-2}meV^{-1}
Level spacing	$1/\rho(E)$	3.57	μeVμm^2
Fermi wave vector	$k_F = (4\pi n_s/g_s g_v)^{1/2}$	1.1×10^6	cm^{-1}
Fermi energy	$E_F = (\hbar k_F)^2/2m^*$	7.0	meV
		81	K
Fermi wavelength	$\lambda_F = 2\pi/k_F$	56	nm
Fermi velocity	$v_F = \hbar k_F/m^*$	1.9×10^7	cm/s
Scattering time	$\tau = m^*\mu_e/e$	40	ps
Mean free path	$l = v_F\tau$	10	μm
Resistivity	$\rho = (n_s e\mu_e)^{-1}$	30	Ω per square
Diffusion constant	$D = v_F^2\tau/2$	7×10^4	cm^2/s
Thermal diffusion length	$l_T = (\hbar D/kT)^{1/2}$	5×10^3	$\text{nm}/\sqrt{\text{T}}$
Cyclotron energy	$\hbar\omega_c$	1.73	meV/B
		20	K/B
Cyclotron radius	$l_c = \hbar k_F/eB$	70	nm/B
Magnetic length	$l_m = (\hbar/eB)^{1/2}$	26	$\text{nm}/\sqrt{\text{B}}$
Zeeman energy	$g^*\mu_B B$	25.5	μeV/B
		296	mK/B

Table 2-1. Typical parameters of a 2DEG formed in a GaAs/AlGaAs heterostructure. The 2DEG sheet density and mobility are taken as $n_s = 2 \times 10^{11}$ cm^{-2} and $\mu_e = 1 \times 10^6$ cm^2/Vs, respectively. The units of B are Tesla, and the units for T are Kelvin. (Table courtesy of S. Cronenwett; Adapted from Ref. [20]).

(a)

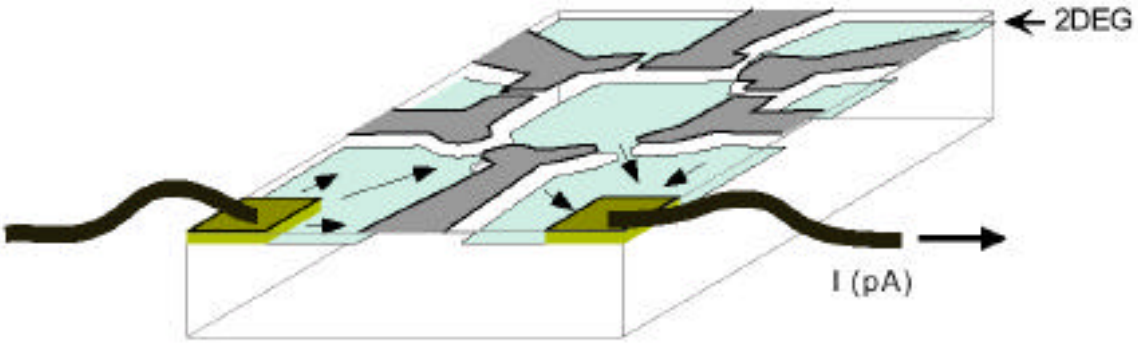

(b)

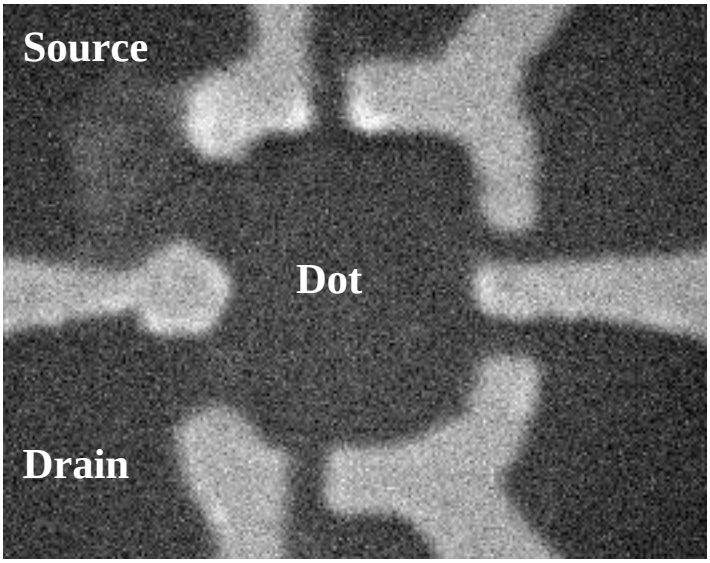

Figure 2-2. a) Schematic 3D view of Dot 4 formed by six gates (gray) on the surface of a GaAs/AlGaAs wafer. The 2DEG, shown in blue, exists slightly below the surface at the interface plane except immediately beneath the negatively biased depletion gates. A current can be passed through the device via the ohmic contacts (gold). Current flows only through the two openings indicated with the black arrows; all the other spaces between gates are fully depleted. b) A scanning electron micrograph (SEM) of a quantum dot. The gates forming the tunneling barriers are colored gold. The 2DEG regions forming the source, drain, and dot are colored in blue. (Figure courtesy of S. Cronenwett).

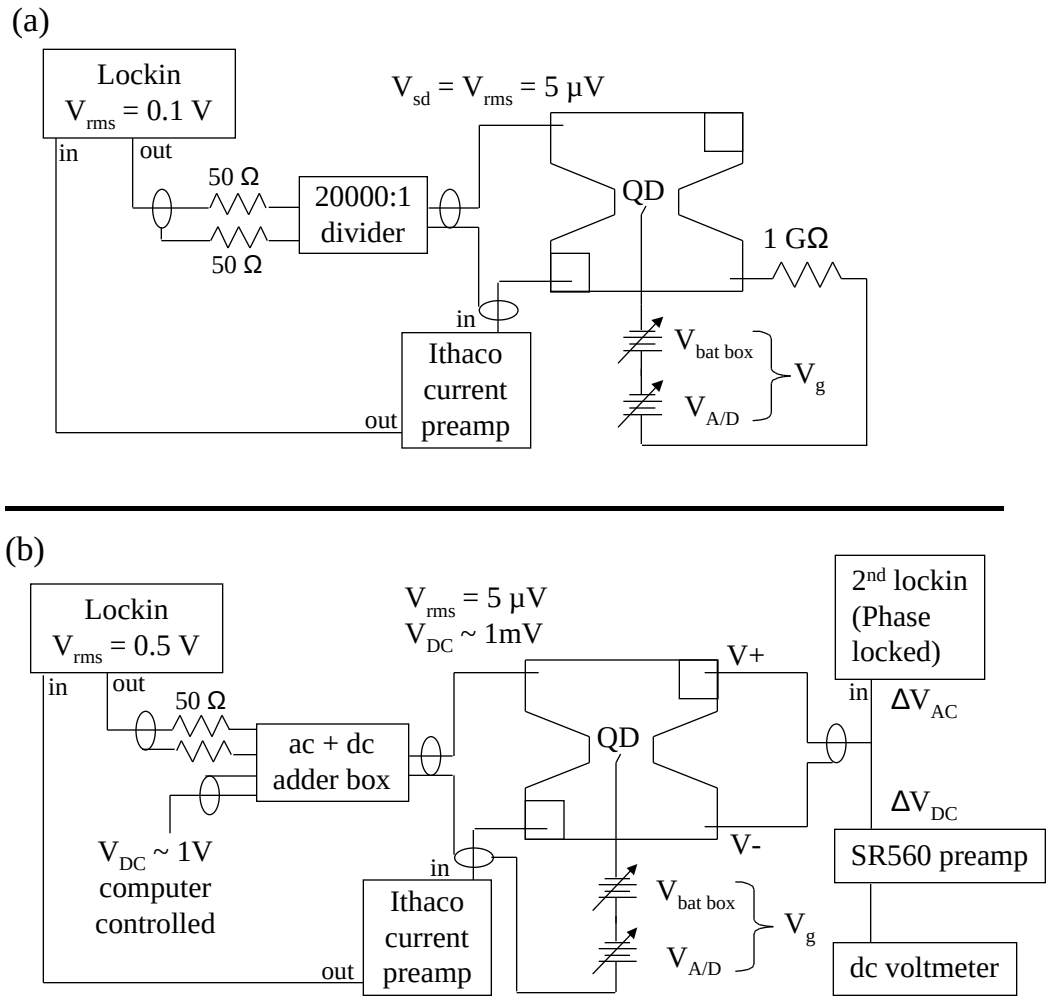

Figure 2-3. Circuit diagram of 2- and 4-wire voltage bias measurements. a) A simple 2-wire measurement consists of a lockin sourced ac voltage, divided down to the desired V_{AC} ~ μV's. The circuit is completed with an Ithaco 1211 current preamp connected to an ohmic in the drain. The output of the Ithaco feeds into the lockin to measure the current. The gates are biased relative to the drain ohmic contacts, through a GΩ resistor to prevent current leakage. b) The 4-wire voltage bias measurement includes separate voltage sensing lines which feed into a second lockin, phase locked to the first, and an optional dc voltmeter. This circuit also shows a finite dc source-drain bias voltage added to the ac voltage. At a frequency of 13 Hz, the ac + dc adder box contains voltage dividers of 100,000:1 and 1000:1 for the ac and dc components respectively. A circuit diagram of the ac + dc adder box can be found in Appendix C. (Figure courtesy of S. Cronenwett).

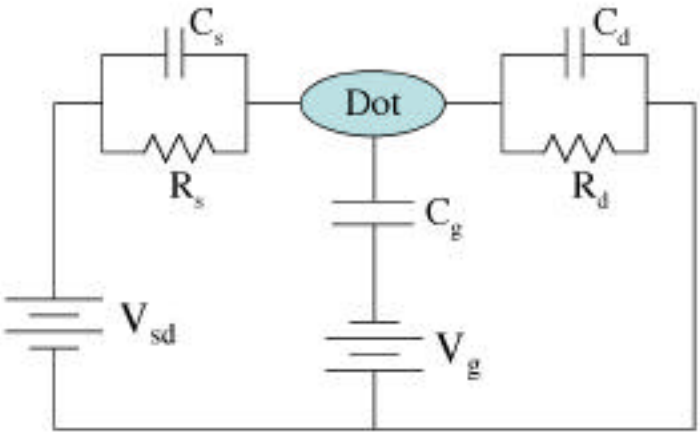

Figure 2-4. Schematic representation of a quantum dot in the CB regime. The dot is connected to the source and drain via a capacitive and resistive element. Dot is connected to surface gate(s) only capacitively. (Figure courtesy of S. Cronenwett).

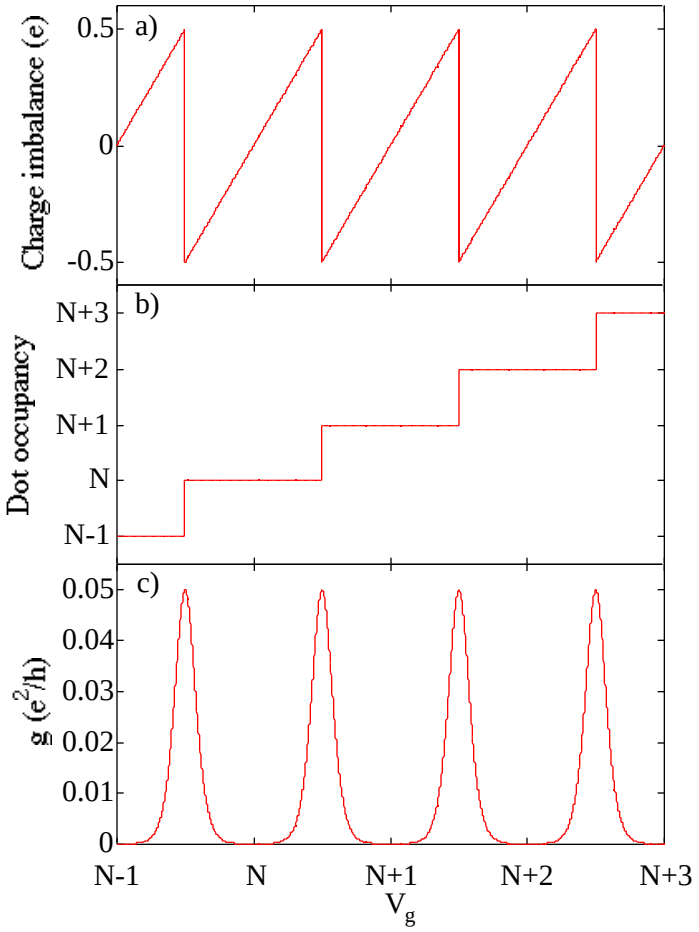

Figure 2-5. Charge imbalance, dot occupancy and conductance. a) The charge imbalance between the quantum dot and the source/drain is shown as a function of V_g. b) The number of electrons on the dot is quantized. c) Coulomb blockade conductance peaks appear at points of degeneracy where the dot occupancy is allowed to change by one. Transport occurs via single electron tunneling ($N \rightarrow N+1 \rightarrow N \rightarrow N+1 \rightarrow \cdots$) in isolated quantum dots at low temperatures and low voltage bias.

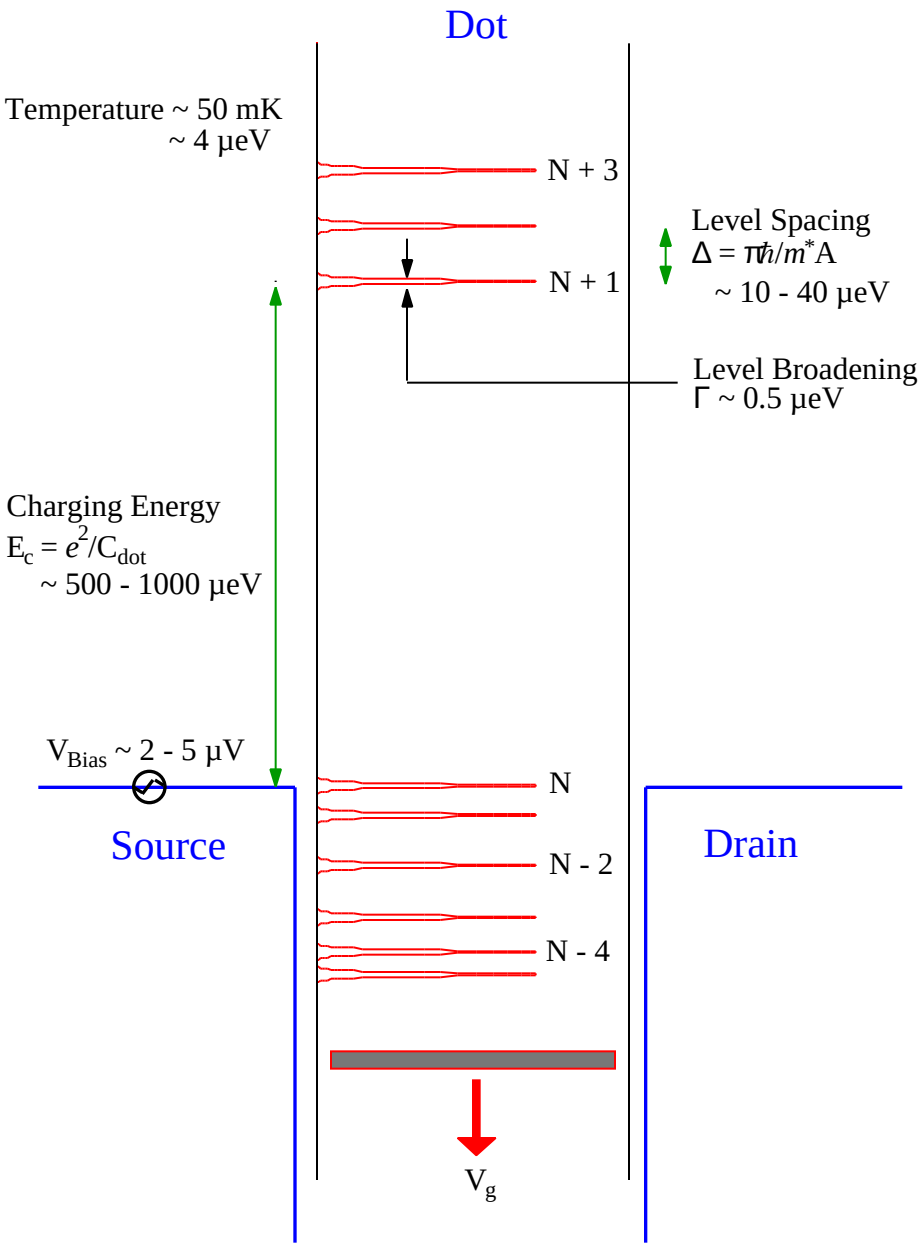

Figure 2-6. Quantum dot energy scales. A schematic representation of the quantum dot level spectrum in the CB regime is shown above. The levels within the dot are broadened due to coupling between the device and the leads; the intrinsic width of the levels is ~ 0.5 μeV. The electron temperature within the dot is ~ 4 μeV. The spin-resolved single particle level spacing is 10 – 40 μeV for devices studied in this thesis. For the same devices, the charging energy E_C ranges from 500 – 1000 μeV. Unless otherwise indicated, an applied ac bias of magnitude 2 – 5 μV was used to measure the differential conductance through the quantum dot.

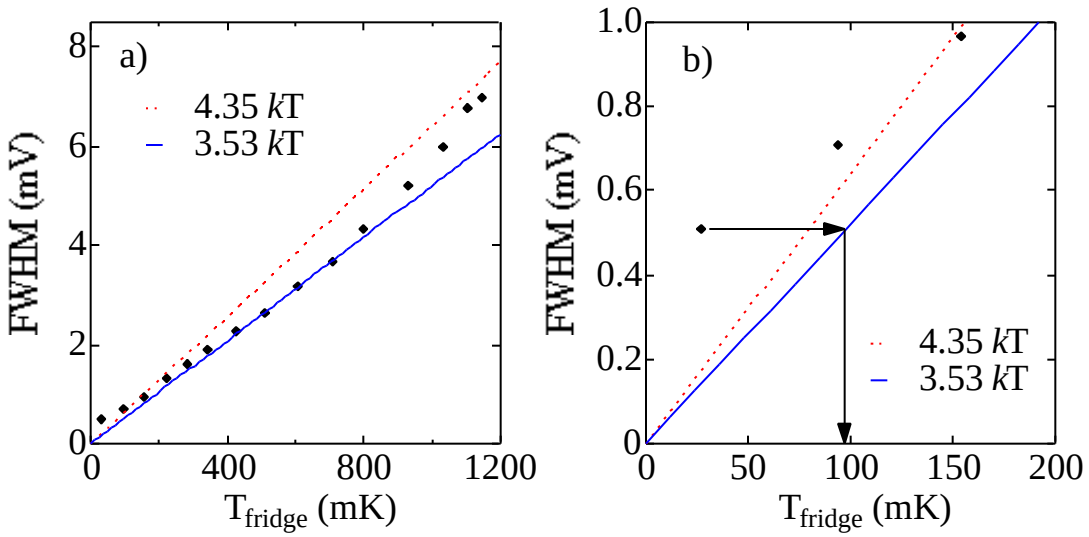

Figure 2-7. Temperature dependence of CB peak FWHM in Dot 4. a) Cross over from 3.53 *kT* dependence to 4.35 *kT* dependence at higher temperatures. Low temperature FWHM does not follow linear prediction due to decoupling of the quantum dot temperature from fridge temperature. b) Zoom-in of (a) plot. Device temperature extracted from base temperature FWHM is approximately 100 mK for this device.

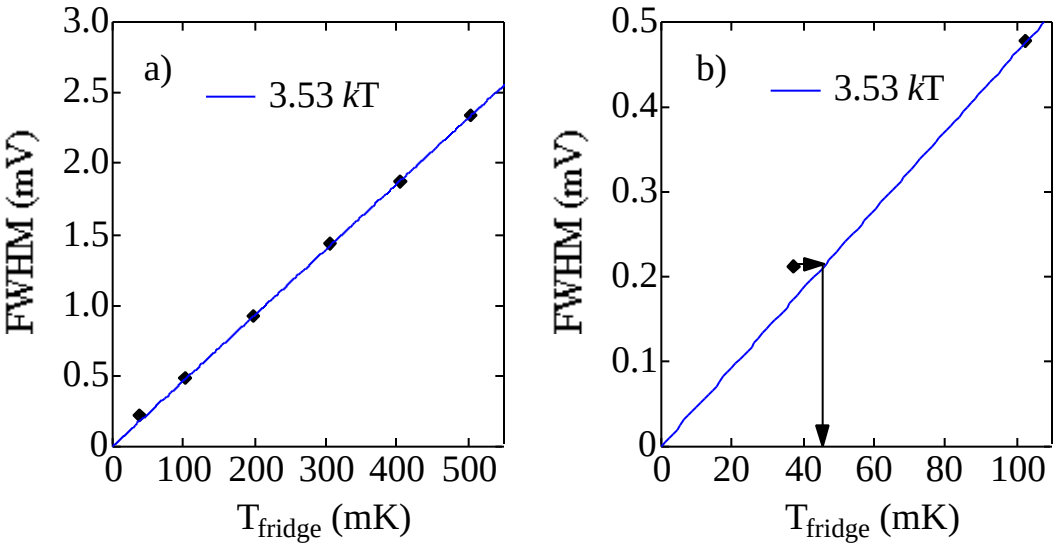

Figure 2-8. Temperature dependence of CB Peak FWHM after improved thermal sinking and RC filtering of the device leads (Dot 5). a) Data showing linear FWHM dependence. b) Zoom-in of (a) data; measured device temperature is ~ 45 mK.

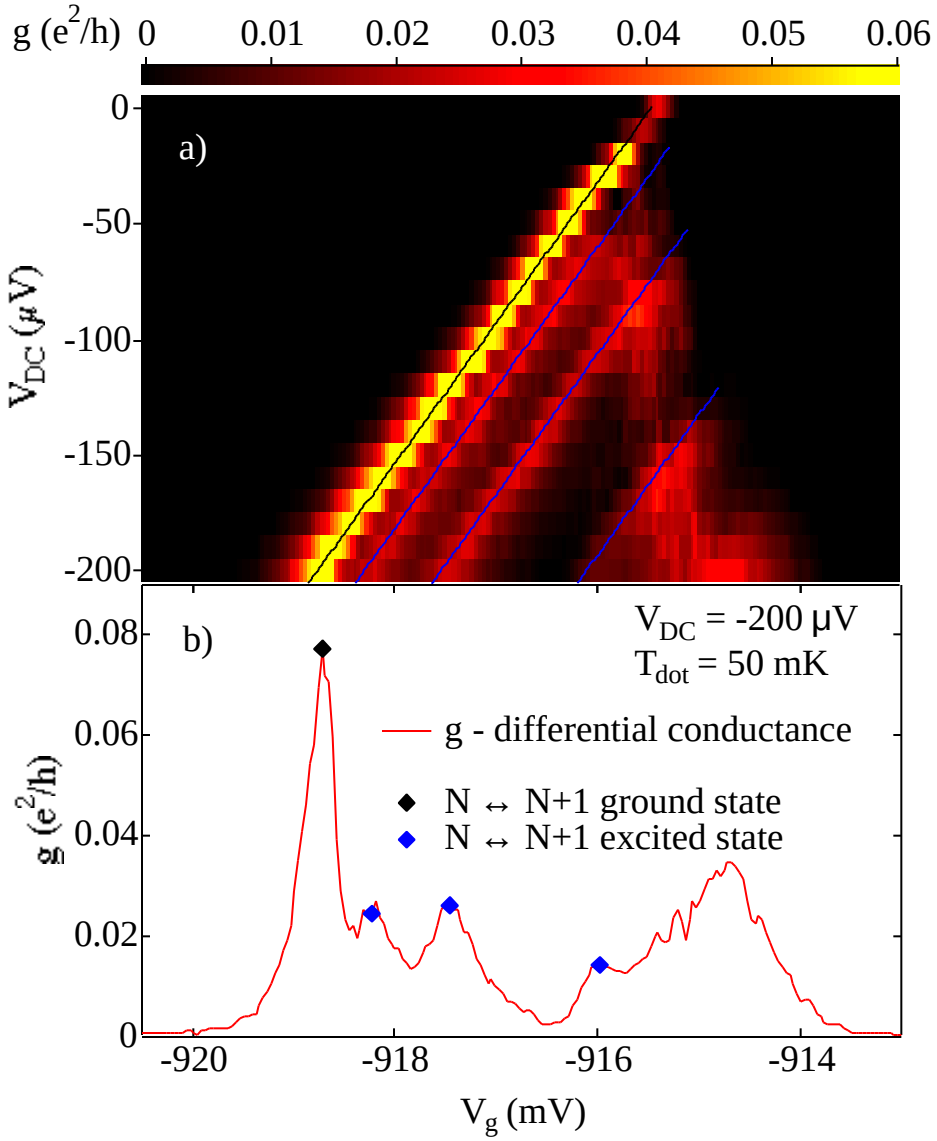

Figure 2-9. Finite bias measurement for Δ. a) The differential conductance through Dot 5 versus applied dc bias. The black line represents the CB peak associated with transitions between N and $N+1$ ground state levels of the quantum dots. The blue lines represent CB peaks associated with transitions between the N ground state level and $N+1$ excited levels of the quantum dot. b) A slice of the data shown in (a) taken with V_{DC} = -200 μV. Measured spacings in V_g between adjacent peaks (black and blue diamonds) are multiplied by η to extract an average Δ = 20 μeV.

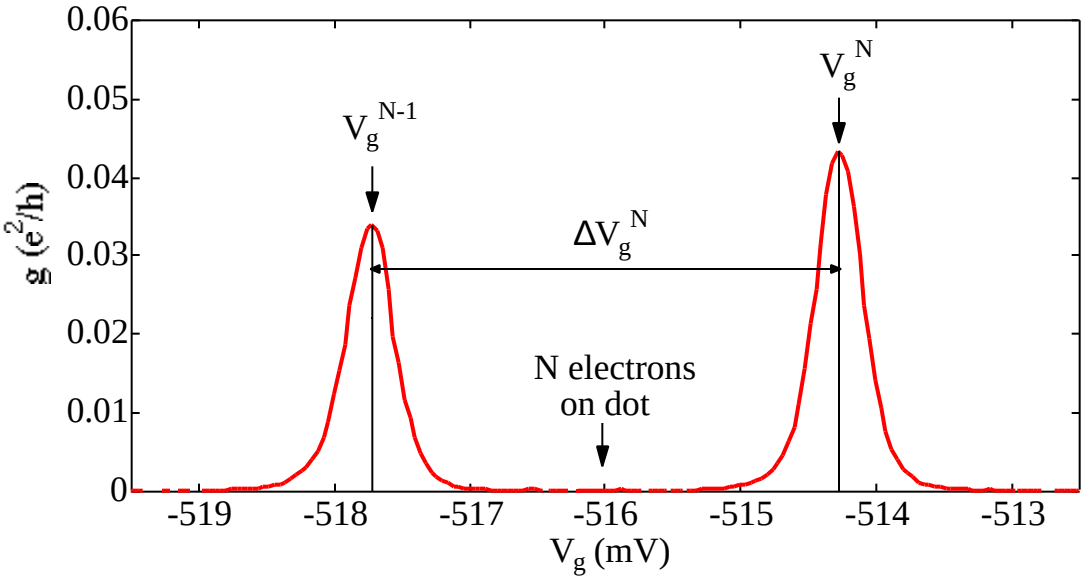

Figure 2-10. Relating E_C to ΔV_g. Two adjacent CB peaks from Dot 5. The peak on the left (right) corresponds to the $N-1 \leftrightarrow N$ ($N \leftrightarrow N+1$) degeneracy condition. In between the peaks, the number of electrons on the quantum dot is fixed to N.

Parameter	dot 1	dot 2	dot 3	dot 4	dot 5	dot 6	dot 7
A (μm^2)	0.17	0.20	0.32	0.34	0.38	0.47	0.50
d (Å)	900	900	800	800	900	800	900
Δ (μeV)	21	18	11	11	9	8	7
E_C (μeV)	560	760	580	500	380	600	320
N	340	400	960	1000	760	1400	1000

Table 2-2. Measured devices and parameters. Data is given for a typical gate voltage configuration (with a nominal depletion region around the dot perimeter): dot area (A), 2DEG depth (d), mean, spin-resolve level spacing ($\Delta = \pi\hbar^2/m^*A$), charging energy ($E_C = e^2/C_{dot}$) and number of electrons in dot (N). Devices 1, 2, 5, and 7 (3, 4, and 6) have a sheet density $n_s \sim 2\times10^{11}\,cm^{-2}$ ($3\times10^{11}\,cm^{-2}$) and mobility $\mu \sim 1.4\times10^5\,cm^2/Vs$ ($6.5\times10^5\,cm^2/Vs$). The 2DEG for devices 1, 2, 5 and 7 (3, 4, and 6) was provided by C. I. Duruoz and J. S. Harris, Jr. at Stanford (K. Campman and A. C. Gossard at UCSB). Devices 1, 2, 5 and 7 (3, 4 and 6) were fabricated by me (Andy Huibers).

Chapter 3

Mesoscopic Fluctuations of Coulomb Blockade Peak Heights

3.1 Introduction

Low temperature transport measurements in quantum dots show random but repeatable fluctuations in the conductance due to quantum coherence of the electrons[3-8]. These mesoscopic fluctuations exhibit universal features which are associated with the underlying universalities of quantum chaos[9-12]. Previous measurements (mentioned above) have focused on transport measurements in the "open" regime (where the conductance of each lead into and out of the dot is greater than or equal to one quantum of conductance ($2e^2/h$)). The experiment described here investigates the mesoscopic conductance fluctuations observed in "closed" quantum dots (device conductance << e^2/h); fluctuations of this type were alluded to in several earlier CB experiments but were not the primary focus of the experiments[24]. Chang, et al. reported the 1st measurement of the conductance distributions and statistics in the "closed" regime; some of the measurements presented here were reported along side of the measurements presented by Chang, et al.[35]. Statistics of CB peak heights and temperature dependence of B ≠ 0 peak height distribution are discussed below. Measurement of the magnetic field correlation length is also presented.

3.2 Coulomb Blockade Peak Heights: Theory

The measurements presented here examine the statistics of conductance fluctuations in the CB regime. Particularly, the measurements are made in the regime $\Gamma < kT$, $\Delta < E_C$ with an ac bias less than kT, Δ, E_C. In this regime, the conductance is a result of single electron tunneling through the quantum levels of the device. For low temperatures ($kT << \Delta$), the transport occurs through a single level of the device; hence, the statistics of the conductance provides a signature of the statistics of the coupling between the source/drain and the single electron eigenstate corresponding to the level participating in the transport[1, 2].

The statistics of single electron tunneling in the CB regime has been studied using random matrix theory (RMT) and super-symmetry method[36, 37]. Within RMT, the Hamiltonian of the isolated device is described by random matrix from Gaussian orthogonal ensemble (GOE) for zero applied magnetic field and from Gaussian unitary ensemble (GUE) for finite, non-zero applied magnetic field. The symmetry classes are selected to respect the time-reversal symmetry constraint of the Hamiltonian. Transport in the quantum CB regime ($kT << \Delta$) resembles the statistical theory of compound nuclear scattering, with the CB peak heights analogous to Porter-Thompson distributions of the resonance widths. The assumption that the overlap integrals of the dot wavefunctions with the lead wave functions are Gaussian distributed implies that the tunneling rates into and out of the dot Γ_l and Γ_r (proportional to the square of the overlap) are χ^2_ν distributed with $\nu = 2$ for B = 0 and $\nu = 4$ for B ≠ 0. The distributions of Γ_l and Γ_r are given by:

$$P(\Gamma) = \frac{e^{-\Gamma/\bar{\Gamma}}}{\bar{\Gamma}} \quad (B = 0) \qquad [3.1]$$

$$P(\Gamma) = \left(\frac{2}{\bar{\Gamma}}\right)^2 \Gamma e^{-2\Gamma/\bar{\Gamma}} \quad (B \neq 0) \text{ [36].} \qquad [3.2]$$

The CB peak height can be expressed as:

$$g_{\max} = \frac{e^2}{h}\frac{\pi}{2kT}\frac{\Gamma_l\Gamma_r}{\Gamma_l+\Gamma_r} \equiv \frac{e^2}{h}\frac{\pi\bar{\Gamma}}{2kT}\alpha\,, \qquad [3.3]$$

where $\alpha \equiv \Gamma_l\Gamma_r/\bar{\Gamma}(\Gamma_l + \Gamma_r)$ is a dimensionless peak height. The mesoscopic fluctuations in $g_{\max}$ arise from changes in Γ_l and Γ_r with external parameters such as magnetic field (for non-zero applied field), dot shape (for zero and non-zero applied field) and the number of electrons in the

dot. Assuming that the dot leads are statistically independent and identical ($\bar{\Gamma}_l = \bar{\Gamma}_r = \bar{\Gamma}/2$), the distributions of the dimensionless peak heights are given by:

$$P(\alpha) = \sqrt{\frac{2}{\pi\alpha}}\, e^{-2\alpha} \quad (B = 0) \qquad [3.4]$$

$$P(\alpha) = 4\alpha\left[K_0(2\alpha) + K_1(2\alpha)\right] e^{-2\alpha} \quad (B \neq 0), \qquad [3.5]$$

where K_0 and K_1 are modified Bessel functions[36].

The peak height distributions discussed above assume that $kT << \Delta$ and only one level contributes to the measured conductance/transport; the changes to the distributions and the height statistics arising from finite temperature effects has been recently considered by Alhassid, et al.[38]. Their calculation includes transport from more than one level as kT becomes larger than Δ. The calculated peak height distributions and standard deviations for B ≠ 0 are compared to measured distributions below.

Alhassid and Attias show that the generic peak height autocorrelation function $C(\Delta X)$ (where ΔX is a change in any continuously varying parameter which induces a change in Γ_l and Γ_r) is approximated by a Lorentzian squared for B ≠ 0[39]. Taking magnetic field as the continuous parameter, the functional form of the autocorrelation function becomes:

$$C(\Delta B) = \left[1 + (\Delta B / B_C)^2\right]^{-2}. \qquad [3.6]$$

The correlation field length B_C is typically smaller than one flux quantum φ_0 through the dot, $B_C A \sim \kappa\varphi_0\sqrt{\tau_{cross}/\tau_H}$, where $\tau_H = \hbar/\Delta$ is the time scale to resolve individual levels, $\tau_{cross} \sim \sqrt{A}/v_F$ is the time to cross the dot, and κ depends on the dot shape[40, 41]. The measured magnetic field correlation length is compared to B_C from above.

3.3 Coulomb Blockade: Magnetic Field and Dot Shape

Coulomb blockade peak height distributions for B = 0 and B ≠ 0 were measured in Dots 3 and 6 in the regime $\Gamma < kT < \Delta < E_C$. Figure 3-1 shows the temperature dependence of a CB peak line shape as a function of device temperature; the device base temperature in this measurement is ~ 90 mK. The CB peak line shape is accurately described by a $\cosh^{-2}$ functional form. The peak width exhibits the linear dependence on temperature as discussed in section 2.4.2. The measurements were made with an ac voltage bias of 5 μV at 11 Hz.

Peak height statistics were collected by sweeping gate voltage V_{g1} over ~ 25 peaks (see inset Fig. 3-4a). For B = 0 and B ≠ 0, independent ensembles of CB peaks are accessed on gate 1 by changing the shape of the quantum dot by adjusting the voltage applied to gate 2; the use of shape distortion to access independent ensembles was originally suggested by Bruus and Stone[41]. Figure 3-2 shows the effect of shape distortion on the CB peak heights measured by sweeping voltage V_{g1} for two different values of V_{g2}. Changing the value of V_{g2} changes the dot occupancy and/or dot geometry (inducing a change in the couplings Γ_l, Γ_r) to yield a new sample of statistically independent peaks on V_{g1}. For B ≠ 0 statistics, the magnetic field through the dot was varied by more than one B_C to access another independent ensemble of CB peaks with gate 1. The inability to access ensembles at B = 0 using the magnetic field greatly reduces the total possible number of statistically independent CB peak height measurements; this necessitates the use of shape distortion as described already. The peak heights exhibit mesoscopic fluctuations; for fixed magnetic field and fixed V_{g2}, the peak height sequence generated by sweeping gate 1 is repeatable.

Figure 3-3 shows the measured peak height versus magnetic flux for Dot 4. The peak height is symmetric with respect to the origin; mesoscopic fluctuations in the peak height are visible between 5 – 15 φ_0 through the quantum dot. One flux quantum through the dot is equivalent to 12.2 mT based on the area estimate (including depletion). The measured magnetic flux correlation length is 0.8 φ_0 (9.7 mT) compared to 0.2 φ_0 from theory assuming that κ is a factor of order unity. The disagreement in the flux scale remains an unresolved issue within this field.

3.4 Coulomb Blockade Peak Height Statistics: Experimental Data

A plot of the B = 0 and B ≠ 0 peak height distribution is shown in Figure 3-4. The data represents CB peak height data measured from both devices. The measured peak height distributions for B = 0 and B ≠ 0 agree with the predicted functional forms from RMT. The displayed data represents data from ~ 600 peaks (for both B = 0 and B ≠ 0) of which ~ 90 are assumed to be statistically independent.

Although the data displayed in Fig. 3-4 shows excellent qualitative agreement with predictions from RMT, the measured probability distribution for B ≠ 0 has visibly fewer near zero height conductance peaks compared to the RMT predictions. This discrepancy can be quantified

by comparing the measured standard deviation of peak heights with predictions from RMT including temperature.

The investigation of the peak height fluctuation standard deviation is simplified by scaling the predicted RMT peak height distributions to have a mean of 1. This is simply achieved by defining a new scaled dimensionless peak height $\tilde{\alpha} = \alpha / \langle \alpha \rangle$; this forces the distribution $P(\tilde{\alpha})$ to have $\langle \tilde{\alpha} \rangle = 1$. The standard deviation of the new distribution is given by $\sigma(\tilde{\alpha}) \equiv \sqrt{\langle \tilde{\alpha}^2 \rangle - 1} = \sigma(\alpha) / \langle \alpha \rangle$. Figure 3-5 shows a plot of $\sigma(\tilde{\alpha})$ versus temperature for 2 different shape configurations of Dot 1 and one shape configuration of Dot 5. All 3 data sets show the same behavior with increasing temperature. The measured data all have smaller peak height fluctuations than predicted by RMT. The measured peak height distributions (insets Fig. 3-5) also show smaller than predicted standard deviations compared to predicted distributions from RMT. This departure from the finite-temperature RMT prediction is likely due to decoherence effects within the quantum dot; as such, it may provide a novel tool to measure decoherence in nearly isolated structures (similar to measurements in open quantum dots[42]).

The peak height distribution calculated from the combined lowest temperature data (inset Fig. 3-5) reproduces the peak height distribution form observed for B ≠ 0 data in Fig. 3-4. This reinforces the underlying universality of the measured CB peak height statistics. Specifically, the same distribution line shape and standard deviation of peak height fluctuations are measured between 4 different devices fabricated out of 2 different 2DEG samples; moreover, the 2 different 2DEG samples were grown by 2 different groups.

3.5 Conclusions

Experimental evidence is presented for mesoscopic fluctuations of CB peak heights as a function of magnetic field. Shape distortion and magnetic field are used to gather statistics of CB peak heights in various quantum dots. The peak height distributions agree qualitatively with RMT at low temperatures. The peak height distribution width is observed to be smaller than predicted by RMT including temperature. The magnetic field correlation length, extracted from peak height measurements, is approximately 0.8 φ_0 (where φ_0 is one flux quantum through the dot); this field scale is smaller than predicted by theory.

The initial CB peak height distributions were measured by J. Folk[43]. J. Folk, S. Cronenwett and S. F. Godijn assisted with device measurements; A. Huibers assisted in device

fabrication. The 2DEG was supplied by K. Campman and A. C. Gossard from UCSB or C. I. Duruoz and J. S. Harris, Jr. from Stanford.

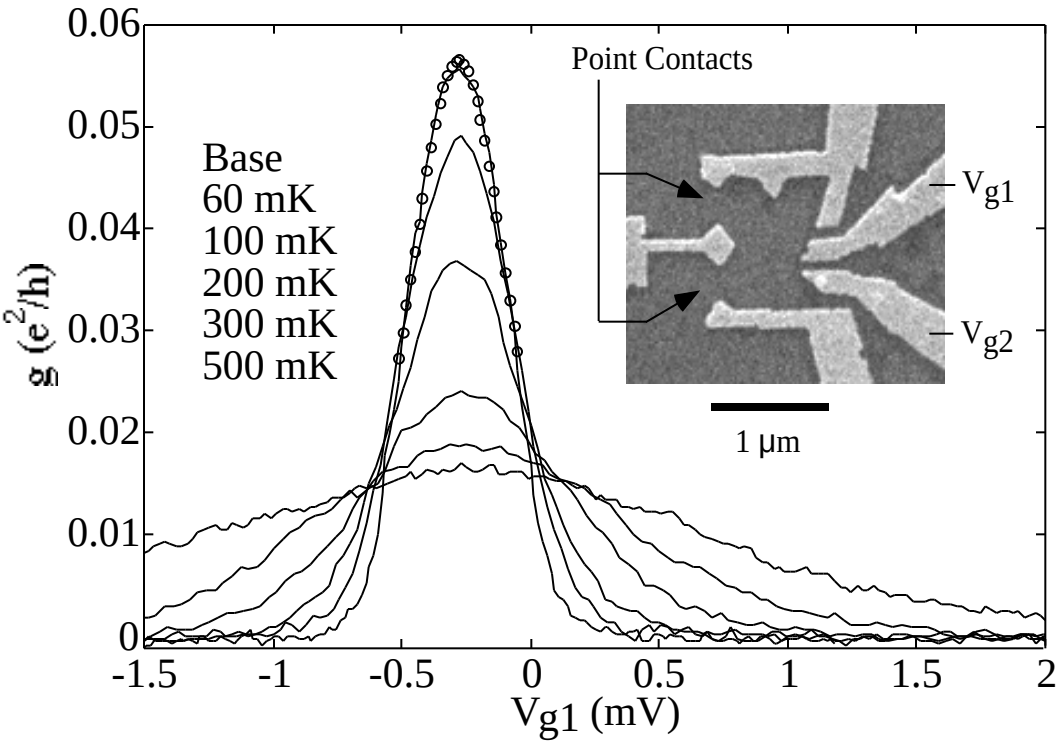

Figure 3-1. Temperature dependence of CB peak line shape. A plot of the conductance through Dot 6 is shown versus the voltage applied to gate 1; the absolute value of the voltage applied to gate 1 is ~ -1 V. The CB peak line shape agrees with Eq. 2.1. At higher temperatures, the CB peak height decreases and the FWHM increases. The inset shows an SEM of Dot 6. The point contacts are tuned to form tunneling barriers into and out of the quantum dot. Gates 1 and 2 can be controlled independently to parametrically change the dot shape.

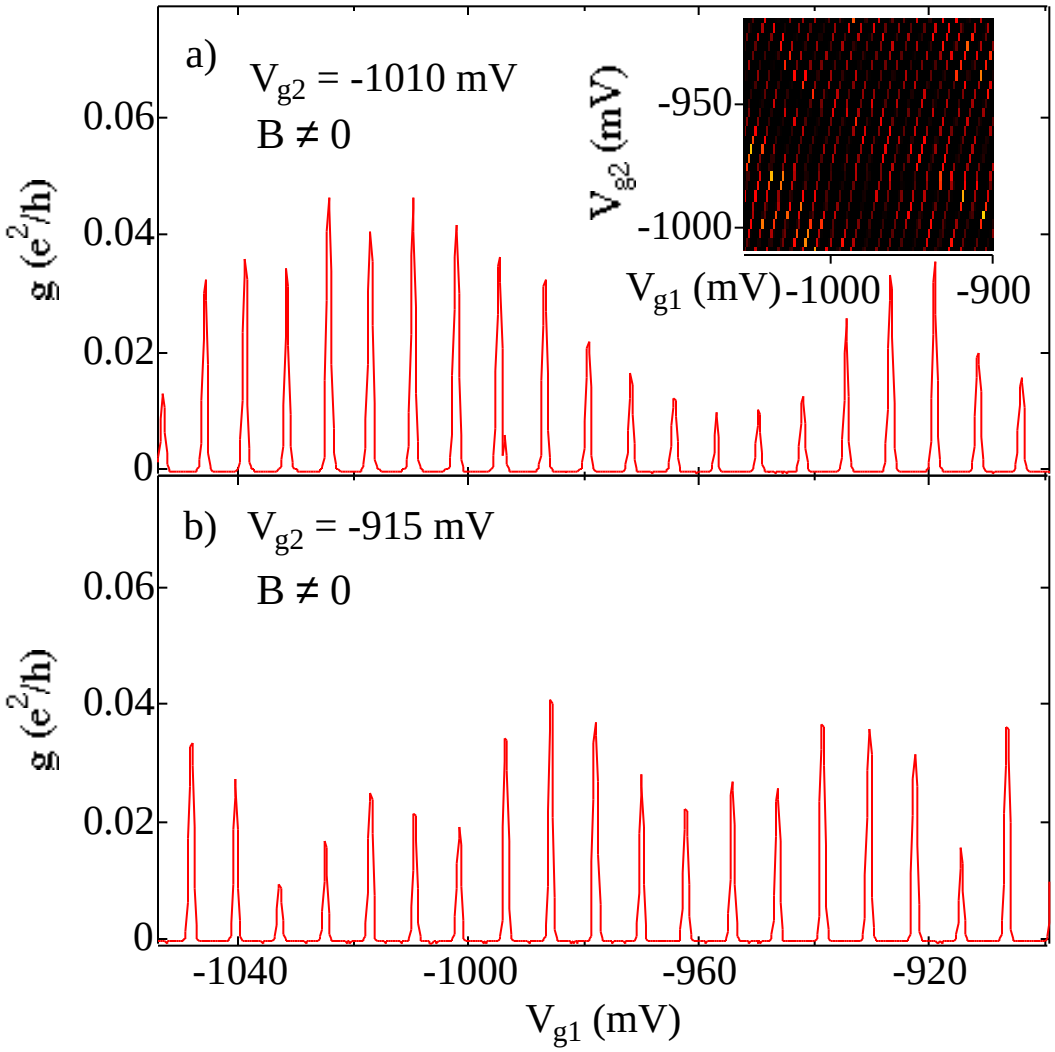

Figure 3-2. Effect of shape distortion. a) CB peaks measured at B ≠ 0 with V_{g2} at –1010 mV on Dot 4. Inset: 2d color scale plot of conductance as a function of V_{g1} and V_{g2}. Dot electron occupancy is approximately the same at the left edge of (a) and the right edge of (b). b) CB peaks measured at the same magnetic field with V_{g2} at –915 mV (change of +95 mV) yields a statistically independent sample of CB peaks.

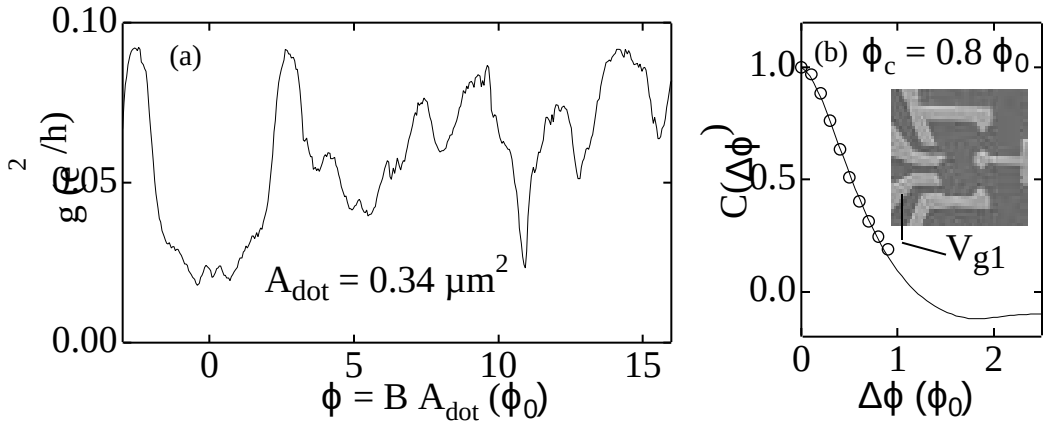

Figure 3-3. Peak height fluctuations and auto-correlation function versus flux. a) Peak height is shown as a function of magnetic flux through Dot 4. Mesoscopic fluctuations of the peak height are observed between 5 – 15 φ_0; the peak height is symmetric with respect to the origin. b) The auto-correlation of the peak height between 5 – 15 φ_0 is plotted. Open circles show best fit Lorentzian squared functional form. Extracted correlation length is 0.8 φ_0 (B_C = 10 mT). Inset: SEM image of Dot 4.

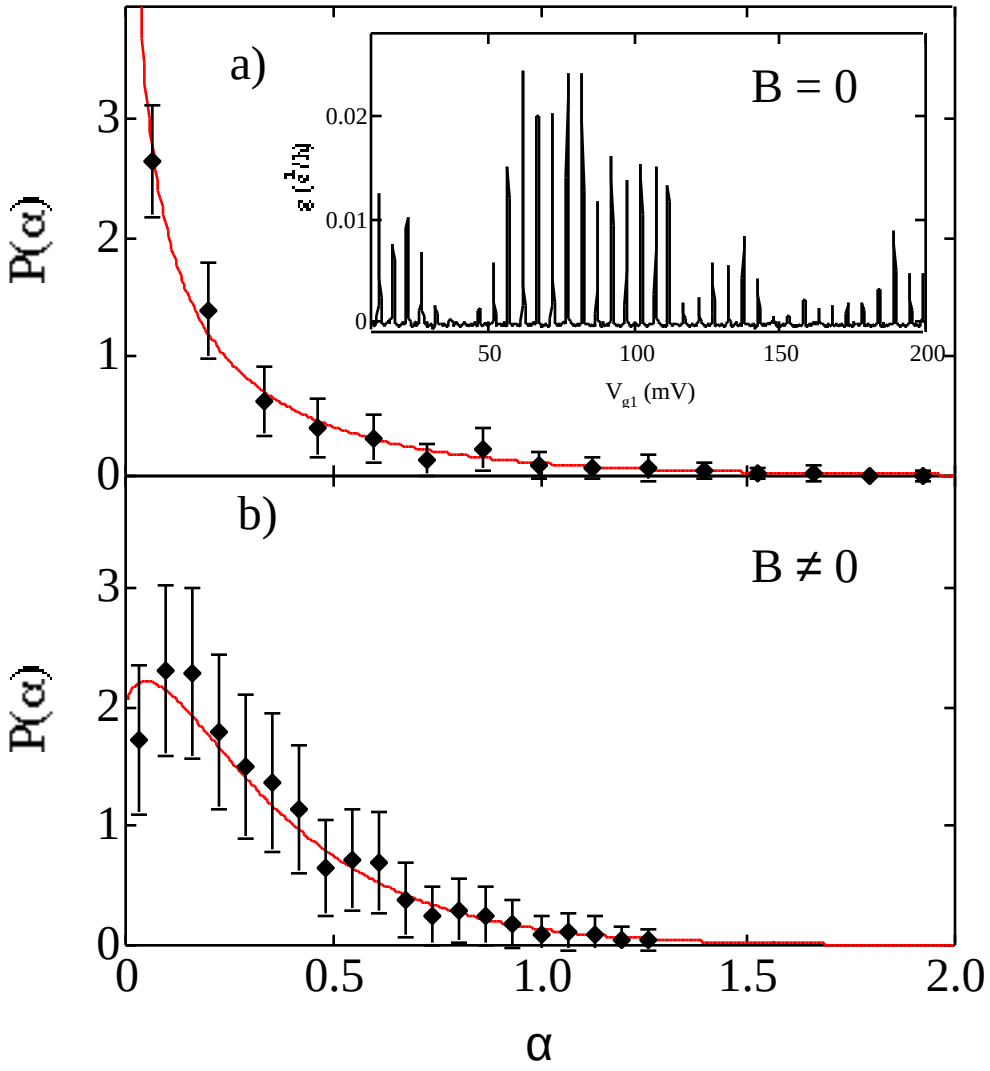

Figure 3-4. CB peak height distributions for B = 0 and B ≠ 0. Peak height statistics from Dots 3 and 6. a) Measured peak height distribution for B = 0 from 600 peaks (~ 90 independent). Inset: Typical scan of CB peaks produced from a sweep over gate 1; note the existence of "missing" CB peaks leading to divergent $P(\alpha)$ at $\alpha = 0$. b) Peak height distribution for B ≠ 0.

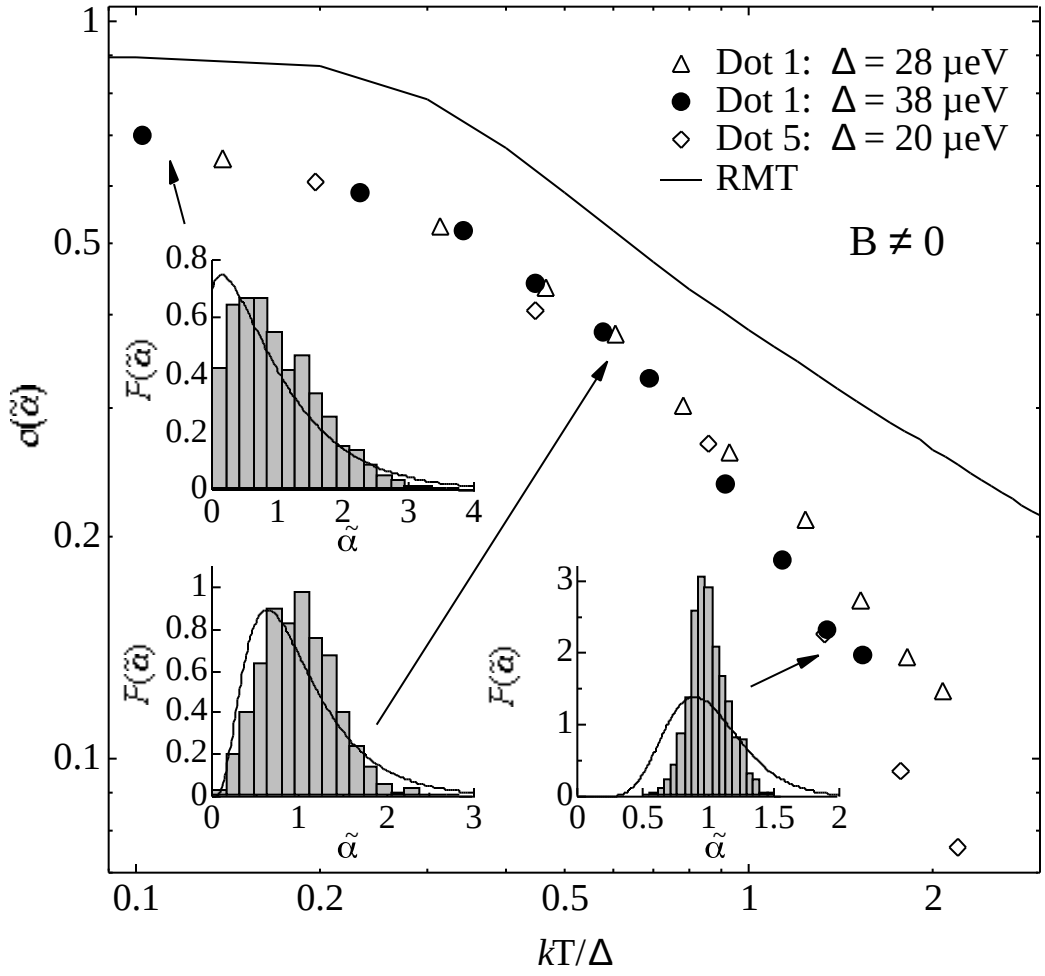

Figure 3-5. Temperature dependence of peak height standard deviations. Normalized peak height distribution width $\sigma(\tilde{\alpha})$ versus temperature is shown for 2 configurations of Dot 1 and one configuration of Dot 5. The width statistics are nearly identical between the device configurations. Insets: Full distributions of normalized peak heights $P(\tilde{\alpha})$ for all dot configurations combined; at kT = 0.1 Δ, kT = 0.5 Δ, and kT = 1.5 Δ. RMT prediction (assuming a uniformly spaced rather than Wigner-Dyson spectrum) is shown in solid curve. Differences between measurements and RMT predictions is likely due to decoherence. The value of Δ is measured from DC bias measurements in the CB regime as described in Section 2.4.3.

Chapter 4

Statistics of Coulomb Blockade Peak Spacings

4.1 Introduction

Measurements of UCF in open quantum dots and statistics of CB peaks heights in isolated quantum dots are observed to be in good agreement with predictions from RMT. Coulomb blockade in isolated quantum dots also provides a measurement of the single electron addition energy as a function of electron number. This measurement is made by converting the CB peak spacings to an energy with the use of η, see Eq. 2.7. Within the "constant interaction" (CI) CB theory, the fluctuations of the CB peak spacings are the same magnitude as the quantum level spacings Δ within the dot; the fluctuations of the charging energy E_C are assumed to be negligible (apart from a slowly varying term depending on dot occupancy N). Several experiments observe that the peak spacing fluctuations are dominated by fluctuations in E_C; the fluctuations are of order 0.1 – 0.15 E_C [44-46]. Statistics of CB peak spacings are studied systematically in seven quantum dots. The temperature dependence of the peak spacing fluctuations is also measured.

4.2 Coulomb Blockade Peak Spacings: Theory

Section 2.4.4 provides the relationship between peak spacings and intrinsic energy scales of the quantum dot. The statistics of $s_N \equiv \beta_{N+1} - \beta_N$ correspond to statistics of the quantum level spacings within the dot. Within spin-degenerate (SD) RMT, s_N is zero for N odd. For N even, s_N is drawn from the Wigner-Dyson distribution. The Wigner-Dyson distributions are given by:

$$P_{WD}(s) = \frac{\pi}{2} s e^{-\frac{\pi}{4}s^2} \quad (B = 0) \qquad [4.1]$$

$$P_{WD}(s) = \frac{32}{\pi^2} s^2 e^{-\frac{4}{\pi}s^2} \quad (B \neq 0) \qquad [4.2]$$

with $s = s_N / 2\Delta$ and $\Delta = \pi\hbar^2 / m^* A$[47]. Using the given Wigner-Dyson distributions, the distributions of s_N are given by:

$$P_{SD}(s) = \frac{1}{2}\left(\delta(s) + \frac{\pi}{2} s e^{-\frac{\pi}{4}s^2}\right) \quad (B = 0) \qquad [4.3]$$

$$P_{SD}(s) = \frac{1}{2}\left(\delta(s) + \frac{32}{\pi^2} s^2 e^{-\frac{4}{\pi}s^2}\right) \quad (B \neq 0) \qquad [4.4]$$

for SD quantum levels within the dot; these distributions are referred to as CI + SDRMT in this thesis. The delta function in the above equations takes into account the spin degeneracy of the quantum levels. The mean value of s_N for both distributions is Δ. The standard deviation of the B = 0 (B ≠ 0) distribution is σ = 0.62 (0.58) Δ; the ratio of the B = 0 standard deviation to the B ≠ 0 standard deviation is ~ 1.1.

Since the experimental data (here and in [44, 45]) does not show any sign of the delta function contribution in the peak spacings, one is forced to consider the CI model without any even-odd structure. The breaking of the spin degeneracy is discussed in [48] and observed experimentally in [15, 16, 28]. The distributions of the spin-resolved (SR) quantum level spacings can be derived from two overlapping Wigner-Dyson distributions [47]. The functional form of the SR level spacing distributions (referred to as CI + SRRMT) is given by:

$$P_{SR}(s) = \frac{\partial^2}{\partial s^2}\left[1 - \mathrm{erf}\left(\frac{\sqrt{\pi}}{4} s\right)^2\right] \quad (B = 0) \qquad [4.5]$$

$$P_{SR}(s) = \frac{\partial^2}{\partial s^2}\left[e^{-\frac{1}{\pi}s^2} - \frac{s}{2}\left(1 - \mathrm{erf}\left(\frac{1}{\sqrt{\pi}}s\right)\right)\right] \quad (B \neq 0). \qquad [4.6]$$

The standard deviation of the CI + SRRMT B = 0 (B ≠ 0) distribution is σ = 0.70 (0.65) Δ; the ratio of the B = 0 standard deviation to the B ≠ 0 standard deviation is ~ 1.1 (nearly identical to the result from CI + SDRMT).

The spin-resolved and spin-degenerate level spacing distributions are shown in Fig. 4-1. The spin-degenerate level distributions show bimodal structure due to the delta function at the origin. As already mentioned for both SR and SD cases, the B = 0 distribution width is wider than the B ≠ 0 distribution width.

The temperature dependence of the CI + SRRMT B ≠ 0 distribution standard deviation can be approximated by thermal averaging the zero-temperature s_N spacings. The finite temperature level spacings are approximated by $y_N = \sum_j w_{N,j} s_j$ with $w_{i,j}$ $\cosh^{-2}\left(|s_i - s_j|/kT\right)$; the functional form of $w_{i,j}$ is chosen to include more contributions from adjacent spacings s_N at higher temperature. Within this model, the CI + SRRMT B ≠ 0 distribution standard deviation is given by $\sigma(T)$ $T^{-1/2}$.

4.3 Coulomb Blockade Peak Spacings Data

Coulomb blockade peak spacings were measured from all seven quantum dots. A typical CB peak scan at B = 30 mT is shown from Dot 1 in Fig. 4-2a. The average peak spacing decreases with increasing number of electrons N in the quantum dot (reflecting an increase in C_{dot}), Fig. 4-2b. To account for this change in the peak spacing, a running average $\langle \Delta V_g^i \rangle$ is found from the best fit line to the peak spacing data; the $\langle \Delta V_g^i \rangle$ is used to defined dimensionless peak spacing fluctuations $\nu = \left(\Delta V_g^i - \langle \Delta V_g^i \rangle\right) / \langle \Delta V_g^i \rangle$. The units of ν are charging energy; the measured peak spacing fluctuations are on the order of Δ / E_C, Fig. 4-2c. A measurement of the noise in the peak spacing data can be made by comparing the peak spacing fluctuations between positive and negative magnetic fields as shown in Fig. 4-2b; the data shown in Fig. 4-2b shows random, repeatable fluctuations in the peak spacing.

Peak spacing statistics from all dots is listed individually in Table 4-1. Statistics for B = 0 were not measured in Dot 1. The listed value of Δ / E_C is calculated from Table 2-1. The

number of statistically independent peak spacings is calculated from the number of peaks in a given scan times the number of scans with characteristically different peak heights. In all cases the measured standard deviation of the peak spacing fluctuations is less than ~ E_C/20 and on the order of Δ/E_C; this is in good agreement with CI + SRRMT. The measured standard deviation for B = 0 is larger than measured standard deviation for B ≠ 0, in agreement with theory. The ratio of the B = 0 standard deviation to B ≠ 0 standard deviation is ~ 1.3 compared to ~ 1.1 from theory. An estimate of the noise in the peak spacing measurement is provided by measuring the anti-symmetric component of the peak spacing fluctuations measured at opposite magnetic field values (as shown in Fig. 4-2b). Devices 2, 6 and 7 exhibit a correlation between enhanced $\sigma_{\text{noise}}(\nu)$ and larger $\sigma(\nu)$.

Combined peak spacing data for Dots 3, 4 and 5 (with similar device parameters) is displayed in Fig. 4-3. Distributions for B = 0 and B ≠ 0 are symmetric in ν and nearly Gaussian. The absence of any bimodal structure in the measured distributions indicates a breaking of spin degeneracy within the dot. For comparison, the bimodal CI + SDRMT distributions with thermal broadening (via convolution of the zero-temperature distribution with a Gaussian of width kT) are shown in the left insets; there is clearly no such structure in the measured spacing distributions. The measured distribution width for B = 0 (B ≠ 0) is $\sigma_{B=0}(\nu)$ = 0.027 ($\sigma_{B\neq 0}(\nu)$ = 0.022); the distribution width from the best fit Gaussian for B = 0 (B ≠ 0) is $\sigma_{B=0}(\nu)_f$ = 0.019 ($\sigma_{B\neq 0}(\nu)_f$ = 0.015) (the subscript f indicates "Gaussian fit"). The difference between measured width and width from best fit Gaussian results from broad tails (see right insets Fig. 4-3). The ratio of the distribution widths is ~ 1.2 – 1.3 (using either the measured width or the width from a Gaussian fit); this is larger than but comparable to the predicted value from CI + SRRMT. The measured distribution widths are much smaller than previous measurements (see top right inset).

Peak spacing distribution for B ≠ 0 from the smallest device (Dot 1) is shown in Fig. 4-4a. The data shows good agreement with the predicted CI + SRRMT distribution after thermal averaging is included; thermal smoothing is applied by convolving the zero-temperature distribution with a Gaussian of width kT. The temperature dependence of the distribution width $\sigma_{B\neq 0}(\nu)$ is shown in Fig. 4-4b for 2 different device configurations of Dot 1. The data shows ~ $T^{-1/2}$ dependence; this is in fair agreement with the results from the thermal averaging model described in the theory section. A more complete model of $\sigma(T)$ has yet to be developed. The

measured width at high temperatures shows the noise floor of the peak spacing fluctuations measurement to be around 0.006 from the saturation value of $\sigma(T)$.

4.4 Conclusions

Measurements made in the course of this thesis work show that the CB peak spacing fluctuations are of the order Δ, much smaller than measured previously in other experiments[44, 45]. Additionally, the measurements show that the levels within the quantum dot are not spin degenerate; CI + SRRMT provides a more accurate picture of the level statistics than CI + SRRMT. There is good agreement between the measured peak spacing distributions and the peak spacing distribution derived from spin-resolved level spacing fluctuations in the absence of E_C fluctuations. The temperature dependence of the peak spacing distribution width is measured for Dot 1; the data shows $T^{-1/2}$ dependence.

There has been recent theoretical work by Usaj and Baranger to investigate the absence of spin degeneracy in the peak spacing data [49]. They calculate the effect of: (1) *e-e* interaction, (2) spectral "scrambling" when adding electrons to the dot (see Chapter 5), (3) shape deformation and (4) finite temperature on the peak spacing distribution in the CB regime. Of these mechanisms, the finite temperature effect proves to be the critical factor in establishing agreement between theory and experiment. The measured data presented here agrees with their results.

S. Cronenwett, J. Folk, S. F. Godijn, and D. Stewart assisted with device measurements; A. Huibers assisted in device fabrication. The 2DEG was supplied by K. Campman and A. C. Gossard from UCSB or C. I. Duruoz and J. S. Harris, Jr. from Stanford.

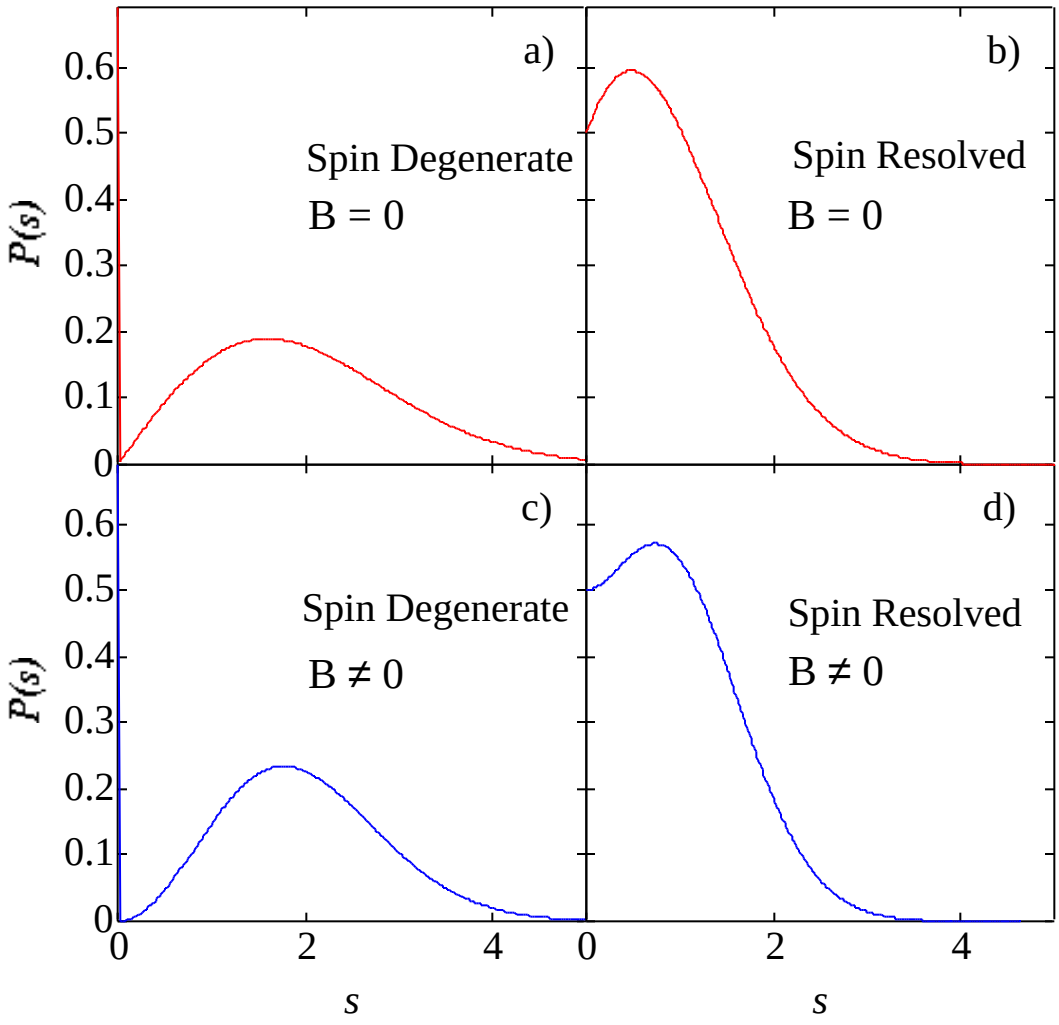

Figure 4-1. Quantum level spacing distributions from RMT. Level spacing distributions for spin degenerate levels are shown in (a) and (c). Level spacing distributions for spin resolved degenerate levels are shown in (b) and (d). All distributions assume zero-temperature inside the quantum dot. In both SR and SD cases, the B = 0 distribution width is ~ 1.1 times the B ≠ 0 distribution width. The mean of all 4 distributions is 1, corresponding to an average level spacing Δ.

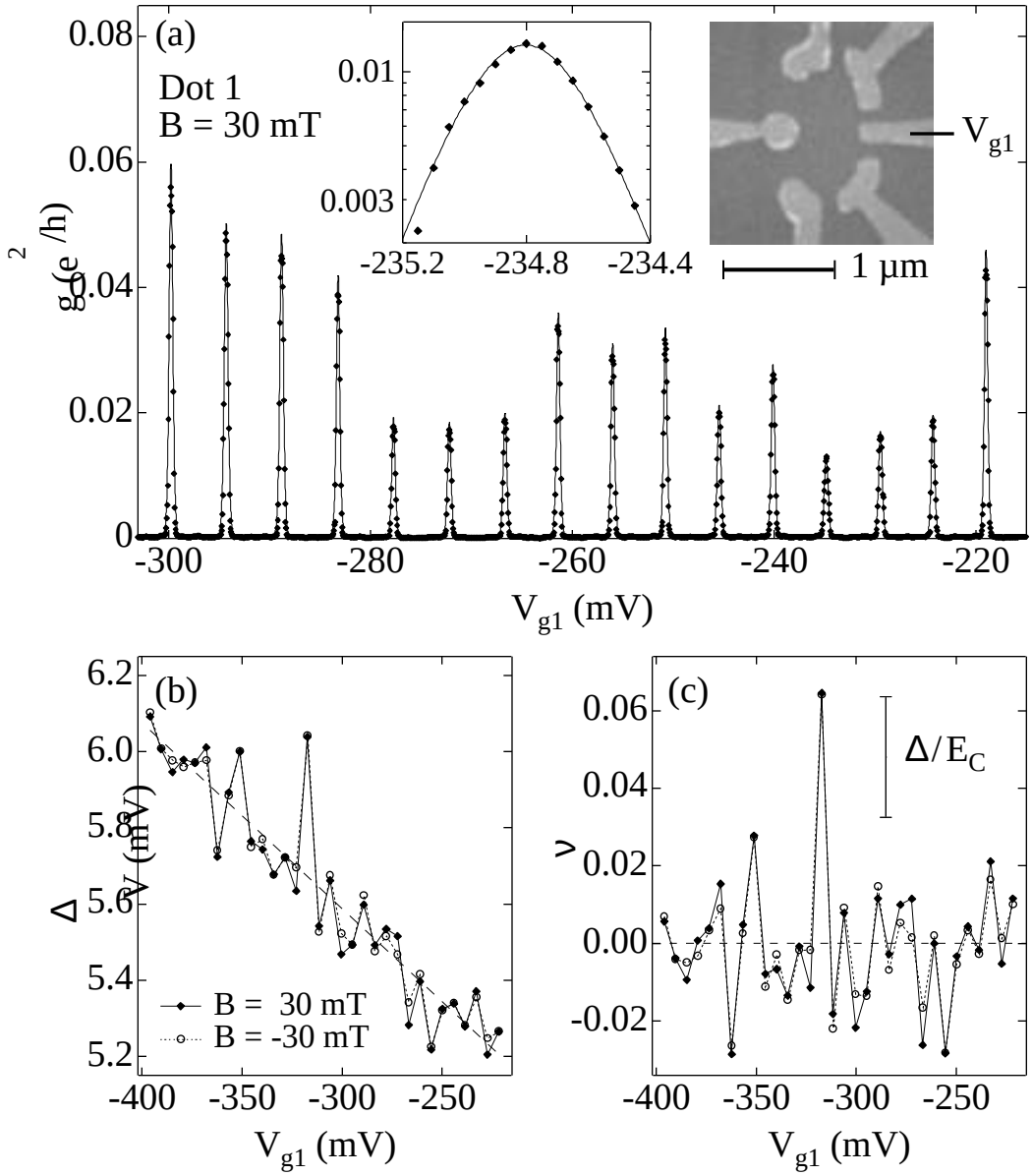

Figure 4-2. CB peak heights and spacings. a) CB peak height data from Dot 1 (diamonds) and best fit to $\cosh^{-2}$ lineshape (solid curve). Insets: Right – SEM image of Dot 1; Left – Detailed view of data and fitted curve on log scale. Peak center location is extracted from fitted curve for each peak. b) Peak spacings extracted from data in (a) at B = 30 mT (diamonds) and B = -30 mT (open circles). Dashed line is best fit to peak spacing data corresponding to $\langle \Delta V_g^i \rangle$. c) Dimensionless peak spacing fluctuations ν as a function of gate voltage V_{g1} from (b). Fluctuations are seen to be on the order of Δ / E_C (vertical bar; see Table 4-1).

Parameter	dot 1	dot 2	dot 3	dot 4	dot 5	dot 6	dot 7
Δ / E_C $(\times 10^{-3})$	36	24	19	22	24	13	22
n_i	190	70	140	830	1300	710	420
$\sigma_{B=0}(\nu)$ $(\times 10^{-3})$	--	48 (7)	38 (2)	25 (2)	25 (3)	43 (2)	56 (3)
$\sigma_{B\neq 0}(\nu)$ $(\times 10^{-3})$	18 (2)	34 (4)	23 (3)	22 (1)	20 (2)	38 (2)	43 (2)
$\frac{\sigma_{B=0}(\nu)}{\sigma_{B\neq 0}(\nu)}$	--	1.3 (0.2)	1.7 (0.2)	1.2 (0.1)	1.2 (0.2)	1.1 (0.1)	1.3 (0.1)
$\sigma_{\text{noise}}(\nu)$ $(\times 10^{-3})$	6	23	15	10	8	25	30

Table 4-1. Measured peak spacing statistics from all dots. Listed parameters: the value of Δ / E_C calculated from Table 2-1, number of statistically independent peak spacings (n_i), measured standard deviation of peak spacing fluctuations $\sigma(\nu)$ for B = 0 and B ≠ 0 with uncertainties in parenthesis, ratio of $\sigma_{B=0}(\nu)$ to $\sigma_{B\neq 0}(\nu)$ (when available) and an estimate of the noise in the measurement as the standard deviation of the noise distribution $\sigma_{\text{noise}}(\nu)$.

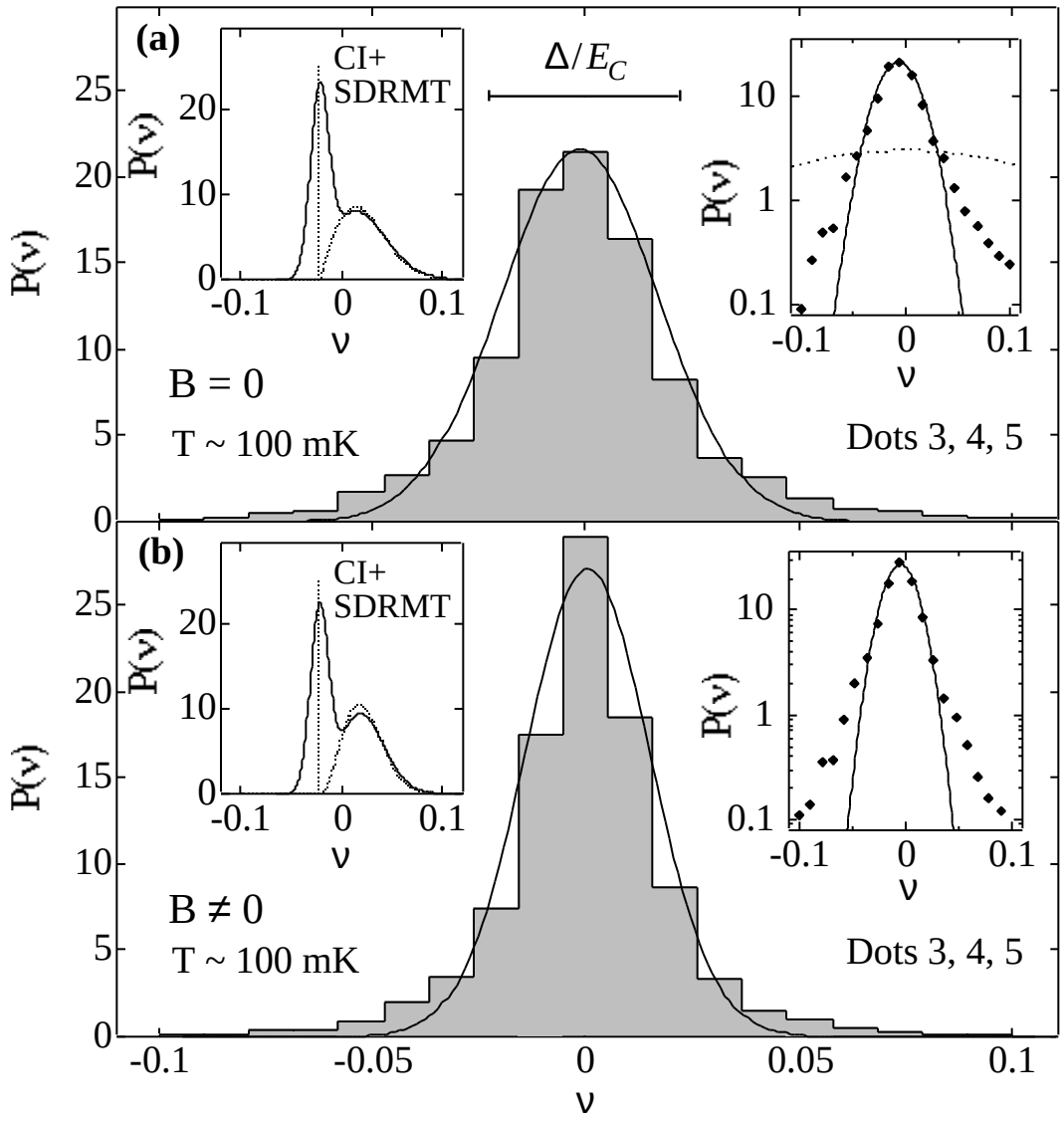

Figure 4-3. CB peak spacing distributions for Dots 3, 4 and 5. a) Measured peak spacing distribution for combined B = 0 data from Dots 3, 4 and 5. b) Measured peak spacing distribution for combined B ≠ 0 data from Dots 3, 4 and 5. Data represents approximately 4300 (10,800) total peaks with ~ 750 (1,600) statistically independent peaks for B = 0 (B ≠ 0). Left insets: CI + SDRMT distributions with thermal averaging show bimodal structure due to spin-degeneracy. Measured distributions do not show any bimodal features. Right insets: Measured distributions (diamonds) and best fit Gaussian on log scale.

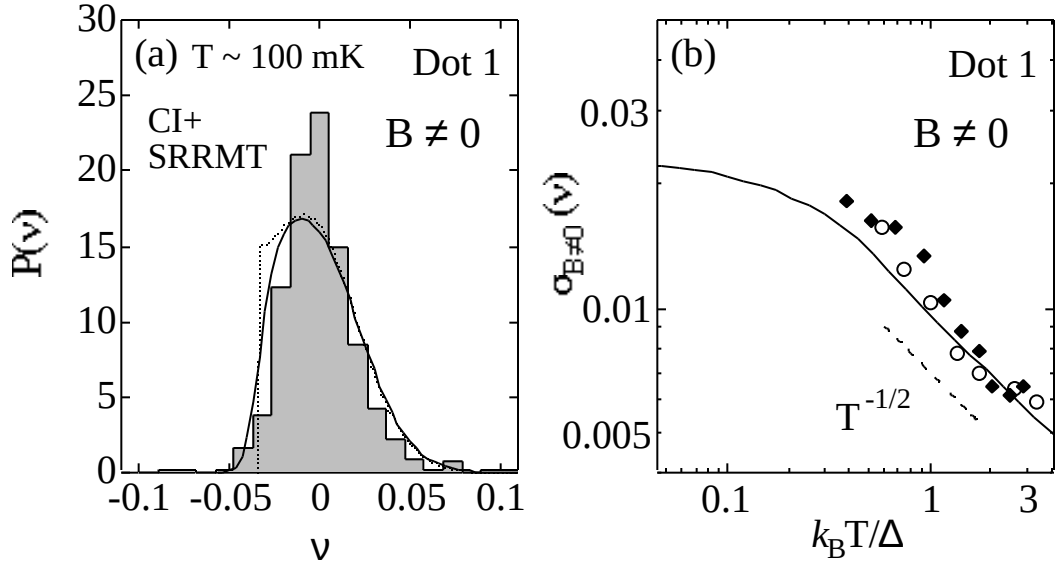

Figure 4-4. Peak spacing fluctuations versus temperature. a) Peak spacing distribution from Dot 1 (bars) compared to CI + SRRMT prediction after thermal smoothing (solid curve). Dotted curve is CI + SRRMT distribution at zero-temperature. b) Temperature dependence of peak spacing distribution width for 2 configurations of Dot 1. Data shows $T^{-1/2}$ dependence. The value of Δ is calculated from area of the dot assuming depletion around the gates.

Chapter 5

Changing the Level Spectrum by Adding Electrons

5.1 Introduction

The magnitude of electron-electron (e-e) interactions within confined systems is the focus of much experimental [44] and theoretical work[48, 50]. The material discussed in this thesis so far has not directly addressed e-e interaction effects. A second hand indication of the e-e interaction magnitude is provided, however, in the peak spacing distribution width measurements. The peak spacing fluctuations observed in Section 4.3 show fluctuations of order Δ. Particularly, the measured fluctuations are much smaller than E_C; fluctuations associated with classical charge rearrangement within the dot are absent. The last statement suggests that the e-e interactions do not dominate CB addition spectrum; however, a more direct study of e-e interaction effects would be useful. A direct probe of the e-e interaction energy scale is made via an investigation of the CB peak height correlation length. Specifically, the temperature dependence of the peak height correlation length provides a novel technique to examine the device level spectrum and couplings for e-e effects.

5.2 Calculation of the Peak Height Correlation Length versus Temperature

As discussed in section 2.4.1, transport on a CB peak in the regime $\Gamma < kT < \Delta < E_C$ is mediated by resonant tunneling through a single level. At higher temperatures (with $\Gamma < \Delta < kT < E_C$), the conductance on a CB peak consists of contributions from kT/Δ quantum levels, and one would expect roughly this many consecutive peaks correlated in height. This assumes that the level spectrum and individual level couplings do not change with the addition of electrons. On the other hand, if the addition of electrons (going from one CB peak to the next) changes the level spectrum and/or individual level couplings of the quantum dot, the peak height correlation length n_c would not grow beyond a certain value. The saturation value would be roughly equal to (but not equivalent to) the number of added electrons required to "scramble" the quantum dot.

The temperature dependence of the peak height correlation length n_c has been derived from RMT distributed peak heights without spectral scrambling within the quantum dot by Alhassid, et al[38]. Within their work (in the regime $\Gamma < kT$, $\Delta < E_C$ with $eV_{bias} < kT$), the on peak conductance is given by:

$$G_{\max} = \frac{e^2}{h}\frac{\overline{\Gamma}}{8kT}\alpha(T), \qquad [5.1]$$

where $\alpha(T) = \sum_\lambda \alpha_\lambda w_\lambda(T)$ is a weighted sum of normalized source-dot-drain conductances and $\alpha_\lambda = 2\Gamma_l^\lambda\Gamma_r^\lambda \Big/ \left[\overline{\Gamma}\left(\Gamma_l^\lambda + \Gamma_r^\lambda\right)\right]$. The dot is assumed to have symmetric leads, i.e. $\overline{\Gamma_l^\lambda} = \overline{\Gamma_r^\lambda} = \overline{\Gamma}/2$. In the regime used in the experiments ($kT, \Delta < E_C$), the weighting function is given by:

$$w_\lambda(T) = 4 f\left(\Delta F_N - \tilde{E}_F\right)\langle n_\lambda\rangle_N\left[1 - f\left(E_\lambda - \tilde{E}_F\right)\right], \qquad [5.2]$$

where ΔF_N is the difference in the canonical free energy of N and $N-1$ non-interacting electrons on the dot, $\langle n_\lambda\rangle_N$ is the canonical occupation of level λ with N electrons on the dot, $\tilde{E}_F = E_F + e\eta V_g - (N-1/2)E_C$ is the effective Fermi energy with V_g tuned between N and $N-1$ electrons on the dot, E_λ is the energy of level λ, and $f(\varepsilon) = 1/\left(1+e^{\varepsilon/kT}\right)$ is the Fermi function. The above equation yields the previously mentioned distributions for α in the regime $\Gamma < kT < \Delta < E_C$.

The calculated peak height sequences are used to extract a correlation length versus temperature. The peak height data of length M is used to calculate a discrete correlation function:

$$C(n) = \frac{1}{M-n}\sum_{i=1}^{M-n}\delta g_i \delta g_{i+n} \Big/ \frac{1}{M}\sum_{i=1}^{M}\delta g_i \delta g_i , \qquad [5.3]$$

where $\delta g_i = (G_{\max})_i - \langle G_{\max}\rangle$. The peak height correlation function is fit to a Gaussian of the form $C(n) = e^{-(n/n_c)^2}$ to extract n_c. This Gaussian functional form is not based on any theoretical model but appears to accurately describe the shape of the calculated peak height correlation function. The calculated $n_c(T)$ from RMT data is shown in Fig. 5-2c. As expected, the correlation length n_c starts from a value close to zero (peak heights uncorrelated at low temperatures) and then transitions to a linear dependence on temperature.

5.3 Measured Peak Height Correlation Length

Coulomb blockade peak height data was collected from Dots 1 and 5 for different temperatures. A typical sequence of peaks at base temperature (~ 45 mK) and 400 mK is shown in Fig. 5-1. The data in Fig. 5-1a shows a short peak height correlation length; peaks which are separated by more than one peak spacing have nearly un-correlated peak height. Same set of peaks at 400 mK are shown in Fig. 5-1b; the correlation length is clearly much larger (~ 3 peaks).

The measured peak height sequences are used to calculate $C(n)$ and n_c for various temperatures. Figure 5-2 shows the measured $C(n)$ curves for Dot 5 and one gate voltage configuration of Dot 1 for various temperatures. For Dot 5, the calculated $C(n)$ curves show a clear increase in n_c for increasing temperature (Fig. 5-2a). The measured values of n_c for Dot 5 and 2 configurations of Dot 1 are plotted in Fig. 5-2c along with the calculated n_c from RMT (as discussed above). The configuration of Dot 1 with the largest Δ, E_C (corresponding to the smallest quantum dot) shows saturation of n_c (to ~ 2) at kT/Δ ~ 0.5. Dot 5 data (largest quantum dot in the data set) does not show saturation of n_c until much larger kT/Δ. The difference in $n_c(T)$ behavior between the different dot sizes suggests that the spectrum and/or level couplings of a small quantum dot are prone to scrambling with fewer number of additional electrons than for a larger dot. The $n_c(T)$ from RMT seems to be the asymptotic behavior of the peak height correlation length in the absence of spectral scrambling.

In order to examine the effect of peak height sequence length M on the observed temperature dependence of n_c, the peak height correlation length was calculated from Dot 5 data (with the longest sequences of CB peak heights) truncated to match the data length from Dot 1 in the configuration producing the smallest quantum dot. The temperature behavior of n_c for Dot 5 data post-truncation does not change compared to pre-truncation. This verifies that the observed saturation of n_c is indeed an effect due to scrambling within the quantum dot upon the addition of electrons and not due to an experimental artifact in the calculation of n_c from the measured data.

All dots show enhancement of n_c at low temperatures compared to predictions from RMT as shown in 5-2c. Several possible explanations for this have been proposed[51-53]. We note that the enhancement of peak height correlation can result from similar peak heights from spin-paired levels. Such pairs of correlated peaks may appear as adjacent or nonadjacent peaks depending on interaction-induced spin splitting. The inset in Fig. 5-2c shows one such pair of adjacent peaks with similar peak heights from Dot 2.

5.4 Conclusions

Measurement of CB peak height correlation length for 3 devices compared to predictions from RMT provides evidence of a changing spectrum and/or level couplings with the addition of electrons. Smaller dots are more prone to scrambling than larger quantum dots as evidenced by smaller values of n_c at saturation. The observed scrambling is evidence of e-e interactions as added electrons change the level spectrum and/or level couplings within the quantum dot. Enhanced peak height correlation is observed compared to RMT at low temperatures. The enhancement of n_c is noted to arise from similar peak heights from spin-paired levels.

D. Stewart assisted with device measurements. The 2DEG was supplied by C. I. Duruoz and J. S. Harris, Jr. from Stanford.

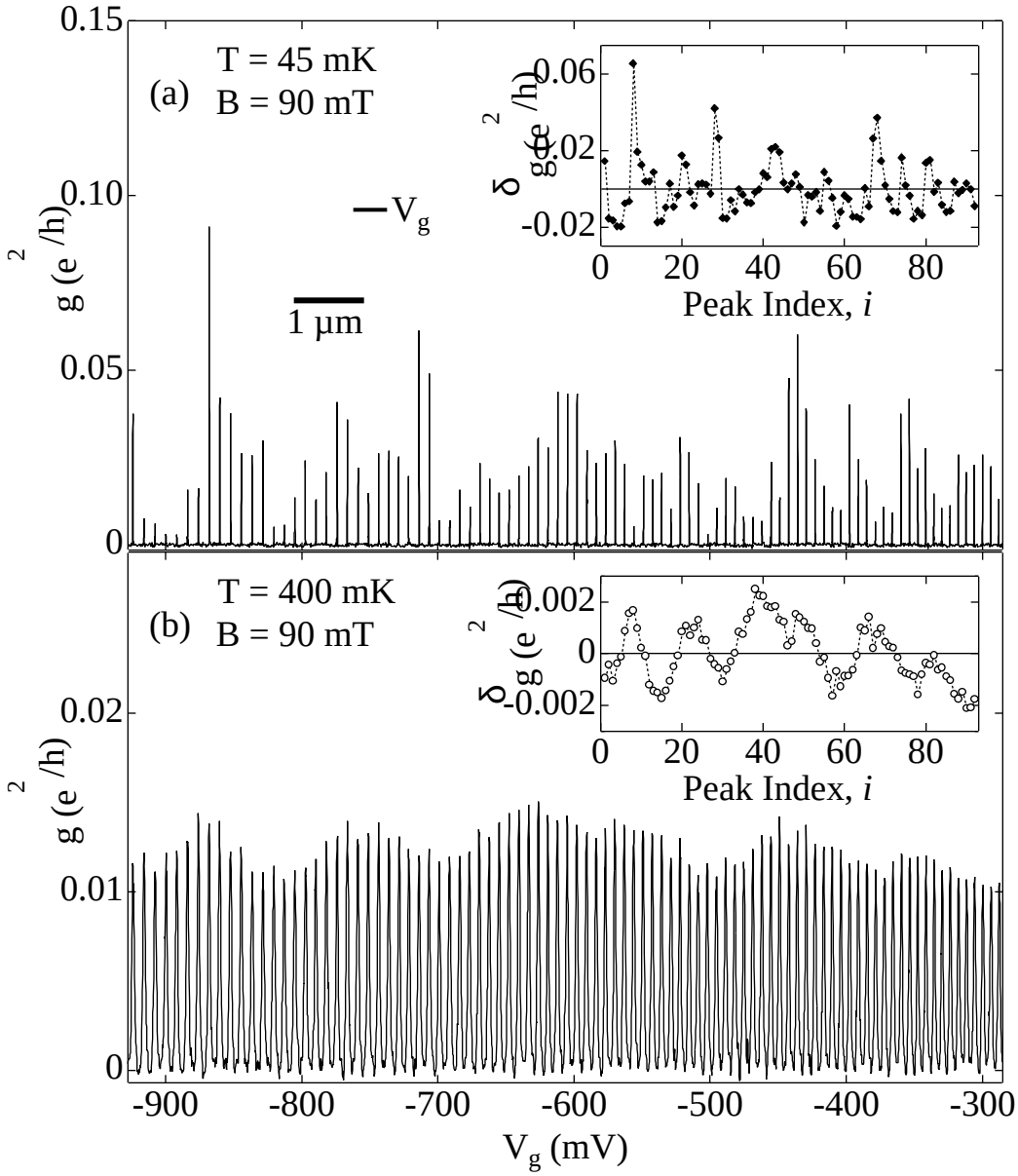

Figure 5-1. CB peak height sequence from Dot 5 for two different temperatures. a) Peak height sequence at T ~ 45 mK. Note that the peak height correlation length is ~ 1. b) Peak height sequence at T = 400 mK. Data shows enhanced peak height correlations compared to data in (a). Insets: Extracted peak height fluctuations data δg used to calculate $C(n)$.

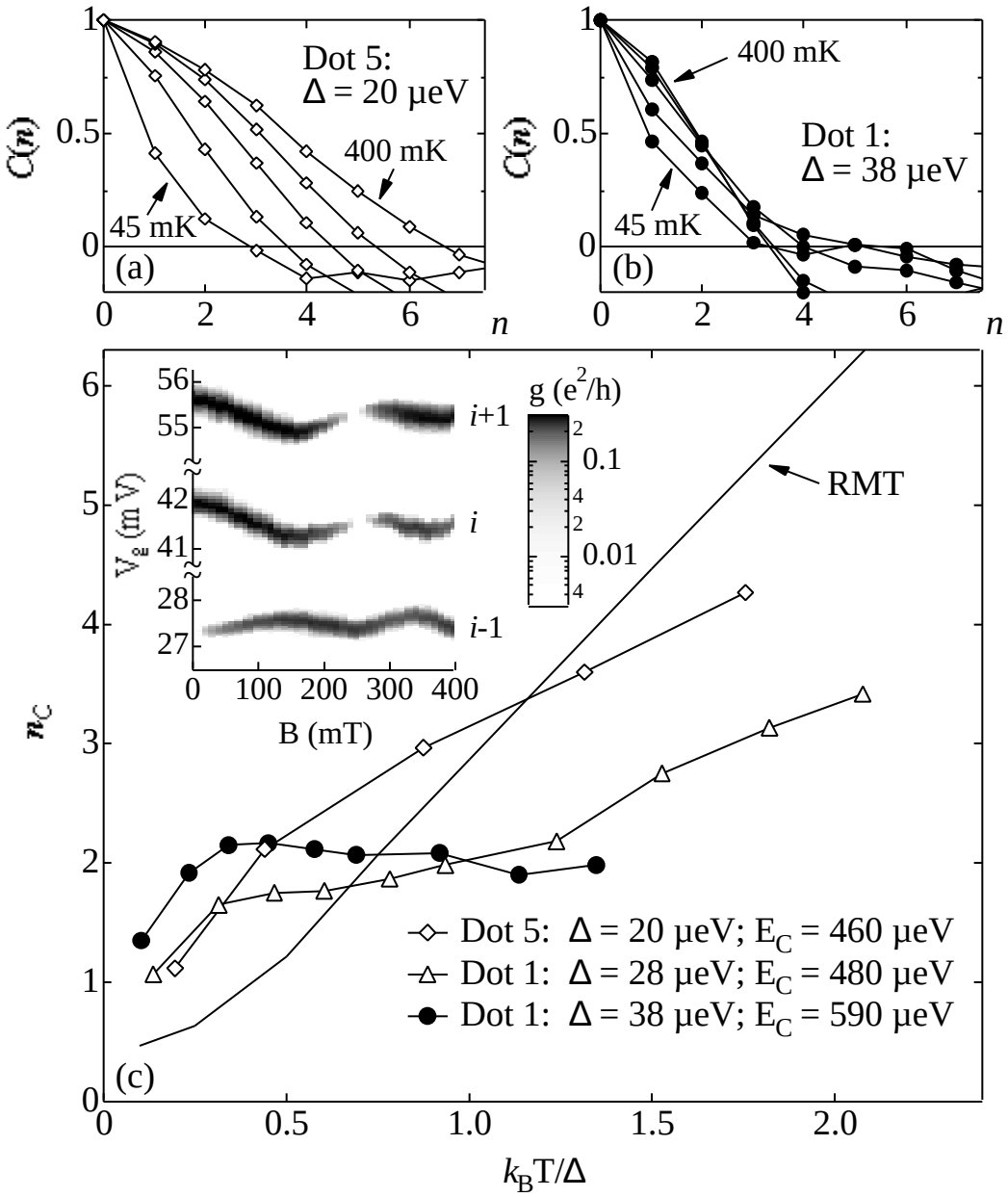

Figure 5-2. CB peak height correlation data: $C(n)$ and n_c. a) Measured $C(n)$ from Dot 5 at 45, 100, 200, 300 and 400 mK. Data shows increasing n_c with increasing temperature. b) Measured $C(n)$ from Dot 1 at 45, 100, 200, 300, 400 mK. Data shows saturation of n_c at higher temperature. C) Measured n_c from 3 data sets and RMT calculations. Saturation of n_c is seen at higher temperatures for the smallest device (solid circles). Enhanced n_c at lower temperatures is observed in measured data compared to RMT. Inset: Example of similar peak heights from adjacent spin paired peaks from Dot 2. Measured values of Δ and E_C are provided in the figure legend.

Chapter 6

Conclusions

6.1 Summary

The focus of this thesis work has been the analysis of statistical data gathered via transport measurements in the CB regime. The measured peak height data shows universal features in the distribution line-shape and distribution width as measured over different devices on different 2DEGs. Moreover, the distribution line-shape and width agree qualitatively with an RMT based model. The discrepancy between the measured peak height statistics and RMT points to a possible dephasing contribution which leads to the reduced distribution width when compared to theory. This reduction in the UCF variance has been observed in "open" quantum dots and used to extract a dephasing time in that regime[7, 42]. Comparing peak height data between devices 1 and 5 in Fig. 3-5 to peak height correlation length n_c data (Fig. 5-2) from the same devices, one can conclude that the peak height statistics are not sensitive to spectral scrambling.

The measurement of peak spacings statistics in the CB regime provides clear evidence of broken spin symmetry. The measured distributions across many different devices do not exhibit any signs of the bimodality expected from a spin-degenerate system. Additionally, the measured distribution line-shapes and width ratios from B = 0 to B ≠ 0 are in good qualitative agreement with the predicted peak spacing distributions from CI + SRRMT. The measured peak spacing distribution widths are on the order of the single particle level spacing Δ; this measured value is much smaller than 0.1 – 0.15 E_C measured by [44, 45]. The intrinsic device noise may be a contributor to the discrepancy between the measurements presented in this thesis and earlier

measurements. The noise floor in the measurements presented here is well below the signal level as seen in Fig. 4-4. There is one discrepancy observed in the peak spacing measurement. The measured value of Δ is larger by a factor of ~ 2 compared to the Δ calculated from the device area assuming spin-resolved single particle levels within the quantum dot. This suggests that perhaps the value of Δ near the Fermi surface is nearly the spin-degenerate single particle level spacing. A clear theoretical model to account for this observation has yet to be formulated.

The peak height and peak spacing data shows good agreement with predictions from RMT (which assumes a non-interacting single particle model of the quantum dot apart from a fixed or, at most, a slowly varying E_C). The measured peak height correlation length n_c shows evidence of departure from the RMT model. First, the measured peak height correlation length versus temperature has different behavior for different sized devices. This non-universality seems to be arising from an interaction effect which is larger in smaller devices (and, hence, induces increased spectral scrambling). There is also an enhancement of the peak height correlation at low-temperatures which is not captured within the RMT framework. The data shows evidence of spin-paired peaks which leads to the observed increase in n_c for smaller devices.

The work presented in this thesis has been published in various articles. References to the published articles is presented here for completeness [43, 54-56].

6.2 Future Direction

The ability to extract the interaction energy scale in a Coulomb blockaded quantum dot would prove to be extremely valuable to formulate a proper theory of the system which includes interactions. This may become possible via additional experiments which focus on the behavior of n_c for different sized quantum dots. There is also a lot of insight to be gained into dephasing in a quantum system by relating the differences observed in the peak height distribution width compared to RMT predictions. There has been some work towards that end by Folk, et al. in which the difference in average CB peak height between B = 0 and B $\neq$ 0 is used to infer contributions from inelastic scattering or dephasing mechanisms in the quantum dot[57]. The peak height distribution widths may be able to provide a second measurement to estimate these mechanisms within the quantum dot.

Appendix A

Device Fabrication

A.0 Acknowledgement

This section is copied with permission from S. Cronenwett's thesis [58] and then edited to describe my fabrication details.

A.1 Overview

The devices measured in this thesis were fabricated in the cleanroom at Ginzton Laboratories at Stanford University. The fabrication process was developed by myself and the following students in the Marcus group: Andy Huibers, Sandra Godijn, Duncan Stewart and Mike Switkes.

The 2DEG used to fabricate the devices was grown by one of two growers who supply material to the Marcus group. The Gossard group at UCSB is one of the 2DEG providers. The other provider is the Harris group at Stanford. We have found that one particular 2DEG wafer grown in the Harris group (wafer CEM2385A) consistently provided the best measurements (lowest switching noise in the 2DEG). I fabricated Dots 1, 2, 5 and 7 from this "quiet" 2DEG. Andy Huibers fabricated Dots 3, 4 and 6 on 2DEG from Gossard's group. Beginning from an MBE-grown wafer, the outline of the fabrication process is as follows:

1. Cleave a small chip (~ 6 mm x 6 mm) from the wafer.

2. Etch mesas to provide electrical isolation between devices (photolithography).

3. Pattern, deposit and anneal ohmic contacts (photolithography).

4. Pattern and deposit gates which define the device on a 100 μm scale (ebeam lithography).

5. Pattern and deposit bondpads which connect to the small scale gates (optical lithography).

6. Glue chip into carrier and bond to devices of interest.

Figure A-1 shows a quantum dot device at several levels of magnification so that the photo and ebeam lithography steps are all visible. As the general principals of photo and ebeam lithography are relatively common in the mesoscopic community, I will not give a broad overview of these fabrication methods but instead describe the particular recipes that I have used.

A.2 Photolithography

Photolithography was done in the inner "Submicron Room" of the Ginzton cleanroom using a Karl Suss MB-3 photolithography machine with chrome plated glass masks. The general principle involves a photosensitive plastic "resist" that is exposed to light in the desired pattern to create a mask for either etching or metal liftoff. Over the years, a number of different masks were made for various device designs. One of the older, but often used, designs can be seen in Fig. A-2. A single 4" mask is usually made with four quadrants to incorporate multiple patterns necessary for a complete device. From left to right, Fig. A-2 shows the designs for a single device mesa, ohmics, and bondpad interconnects.

The photolithography recipe developed in our group has been optimized to be very reliable and give a large undercut to facilitate liftoff. Without doing an edge bead removal step, the resolution of this process is ~ 3 μm. Because we use ebeam lithography for all our small features, the relatively poor resolution is not a problem. The basic photolithography recipe I have used is the following:

- Three-solvent clean for 5 min each in boroethane (or TCE or other equivalent), acetone, methanol. Use ultrasound if possible (not advised after the fragile ebeam layers have been deposited).
- Hotplate bake, 120° C, 5 min. Place chips on a glass slide on the hotplate.

- Spin Shipley 1813 photoresist at 7000 rpm for 30 sec. This gives a ~ 1 μm thick layer of photoresist, with an edge bead.
- Hotplate bake, 90° C, 20 min.
- Chlorobenzene soak, 15 min. This step hardens the top of the resist so it is less soluble in the developer, leading to a large undercut for liftoff.
- Hotplate bake, 90° C, 5 min. (to remove leftover chlorobenzene solvents).
- Expose desired pattern for 24 sec (power = 16.4). These times will depend on the lamp power and should be checked with a junk chip for every machine and fab run.
- Develop in equal parts DI and Microposit concentrated developer for 50 sec. Rinse in fresh developer solution for an additional 25 sec (1 min 15 sec total). It is always OK to check how the develop is progressing by rinsing the sample in DI, looking under the microscope (with a UV filter in place!!) and then continuing the develop if necessary.
- Oxygen plasma with 100% O_2, at ~ 150 W for 0.09 minutes (in the Ginzton Phlegmatron, 50 % power, 0.09 min) to clean the surface.
- For metal evaporation and liftoff steps, we have always done an oxide removal acid dip. We did a HF dip with 20:1 buffered oxide etch (BOE) for 15 seconds.
- For the bondpad interconnect layer, evaporate 200 Å Cr, then 2500 Å Au using processed cooling water to cool the sample during and after the evaporation. Liftoff in acetone, using ultrasound only as a last resort (as the thinner ebeam metal could come off as well).
- The wet etch and ohmic recipes are described in the following sections.

It is strongly advised to process at least one, preferably two, practice (junk) chips along with any real 2DEG sample. In the steps above, the three-solvent clean and bake can be done simultaneously on the real and junk chips. Then spin the junk chips first, and, if they look good, go ahead and spin the real chip. If the junk chips don't turn out for whatever reason, do not proceed with the real 2DEG. The chips may all be baked together, soaked in chlorobenzene and baked again. All exposures, including edge bead removal, should be done on the practice chips first. If the exposure and develop look good (good undercut for metal liftoff processes), then the real chip can be processed in exactly the same manner. Otherwise, cut your loses, rinse off the photoresist in acetone and start again. This is OK even on the ohmic step provided you have not exposed the real 2DEG yet. After exposing and developing the patterns, the chips (real and junk) can be stored, away from solvent fumes and in the dark, for several days with no ill effects. For

metal liftoff steps, process the junk chips through the plasma etch, oxide acid etch, metal evaporation, and liftoff before following with the real 2DEG. If the first junk chip does not liftoff, try the second. If it looks risky and this is the final bondpads step, your time is better spent redoing the whole process than ruining a set of nearly completed devices. If this is the ohmic step, it's a 50-50 decision.

A.3 Wet Etching

Etching of the mesas is done in a solution of dilute sulfuric acid. The mixture is 1:8:240 of hydrogen peroxide : sulfuric acid : DI water. Always add the hydrogen peroxide to the acid in a graduated cylinder to measure, then pour into the DI water. Mix well. Because an etch step can take several hours, I recommend leaving the etch mixture covered with a cover glass when not in use to prevent non-uniform evaporation which will change the etch rate. Every etch mixture should be calibrated using a patterned junk chip made of good GaAs (not a 2DEG heterostructure, but not unknown junk either). I have always used an Alpha Step profilometer to measure the etch profile. We generally etch all of the AlGaAs layer to the depth of the 2DEG, though a shallower etch is sufficient to isolate devices in most cases.

A.4 Ohmic Contacts

Ohmic contact is somewhat of a mystery; there have been many cases in my experience where, even after following this process on junk and real pieces, I would end up with failed ohmics. I believe that a lot of it has to do with the surface preparation where the ohmic metal goes down and also with the contamination of the ohmics material evaporation boats in the evaporator. For best results, replace the 3 boats with new boats and Nickel, Au and AuGe eutectic

Following the photolithography step for the ohmic contacts, metal is evaporated using either a thermal or ebeam evaporator (or both). I have used 50 Å Ni, 1200 Å AuGe eutectic, 250 Å Ni, and 1500 Å Au deposited in a single thermal evaporator step for the ohmic contact metal. The sample is cooled with chilled water during the evaporation. Liftoff in acetone (should be relatively easy with a large undercut, but ultrasound can be used if needed). After liftoff, the ohmic metal must be annealed into the heterostructure to make contact to the 2DEG. The optimum annealing time and temperature will vary from one heterostructure to the next and should be determined separately for each one. Remember to process a little extra material if using a new wafer so you can cleave a couple rows into small pieces to use for ohmic

development. In general, we have found that this Ni-Au-Ge ohmic recipe yields good electrical contact (< 1 kΩ) when annealed at 410° C for 20 – 50 seconds.

Ohmic contacts on the real 2DEG chip should be tested in a dunker at 4.2 K after annealing to ascertain that they are satisfactory at low temperature0 before proceeding with further processing. I would generally test one or two pairs of ohmics on devices near the edge of the chip as well as one set of four ohmics on a single device (to do a 4-wire measurement of the 2DEG as well). If the ohmics seem questionable, keep checking more until you can decide whether the chip is useable or not. Re-annealing ohmic contacts on a chip is a possible last resort.

A.5 Electron Beam Lithography

Electron beam (ebeam) lithography is used to pattern the fine metal structures that define the gates of the quantum dots and point contacts as well as the larger gate material that connects out to the features of the bondpad photo layer. The lithography process is similar to that used for photolithography: a plastic resist is spun onto the chips, the desired patterns exposed with an electron beam microscope (ebeam), then developed. At Stanford I used the converted Leica Leo Stereoscan 440 electron microscope in the Ginzton cleanroom. Each machine requires different design files and different operation, so I will not discuss details that relate to a particular ebeam system.

The recipe I used consists of a double layer PMMA (polymethyl methacrylate) recipe with a light-weight bottom layer and heavy-weight top layer. The light-weight bottom layer is more soluble in the developer, so gives an undercut. The lithography process is as follows:

- Three-solvent clean, 5 min. each in boroethane (or TCE or equivalent), acetone, methanol. Use ultrasound unless thin metal gates have already been deposited.
- Hotplate bake, 2 min. at 180° C.
- Spin on 550 A of 495K PMMA.
- Hotplate bake, 20 min. at 180° C.
- Spin on 1100 A of 950K PMMA.
- Hotplate bake, 30 min. at 180° C.
- Expose with the ebeam system (at ~ 240 μC/cm^2).
- Develop in a solution of 3:1, isopropanol : MIBK with 1.3% methyl ethyl ketone (MEK) added for 35 sec.

- The developed chip is now ready to be loaded into the evaporator for gate metal deposition. For standard Cr/Au gates, we typically use 25 Å Cr and 120 Å Au. Liftoff in acetone. Use ultrasound as a last resort.

As with the photolithography process described above, I strongly advise the parallel processing of at least one junk chip with every real 2DEG sample. After the resist is spun and baked, the junk chip is used to write an exposure matrix with the ebeam. The exposure matrix should be written at a 4 – 6 doses that span the range you would expect to yield good results given the machine being used (center point at ~ 240 μC/cm^2). Sometimes an ebeam system gives nearly the same results even after several months, while other times you may find exposures change from week to week or worse, day to day. The exposure matrix is also a good opportunity to test all of your device designs to make sure they write as expected. Keep at least one device that you write at every exposure to pick the correct dose. To select the proper exposure, develop the junk chip, evaporate the gates, and view the chip in the SEM. If none of the exposures look good, or devices have not written as expected, repeat the exposure matrix on a second (or third or fourth) junk chip if you have one. If not, clean the PMMA off the real sample and start again, processing more junk chips in parallel. Once a good exposure dose is found, the real chip should be written as soon as possible.

Most ebeam metal layers consist of very small features which define the dot or point contact, as well as larger metal strips which extend the small gates out to the photolithography bondpad layer. These two (or more) sets of gates are typically written at successively lower magnification and, correspondingly, successively higher dosages. Usually, only the resolution and precision of the smallest features are important, so larger gate sets can be overexposed to ensure they turn out.

A.6 Packaging and Wire Bonding

We use PMMA to glue chips to our 28 pin non-magnetic ceramic chip carriers. An advantage of using PMMA as glue means that chips can be easily removed from the carriers by soaking in acetone. I have used an ultrasonic wedge bonder (an old West-Bond model 5416) with 25 μm Au wire to connect the bond pads on the device to the chip carrier pads. I often use a little heat, ~ 70° C, on the sample chuck during wire-bonding.

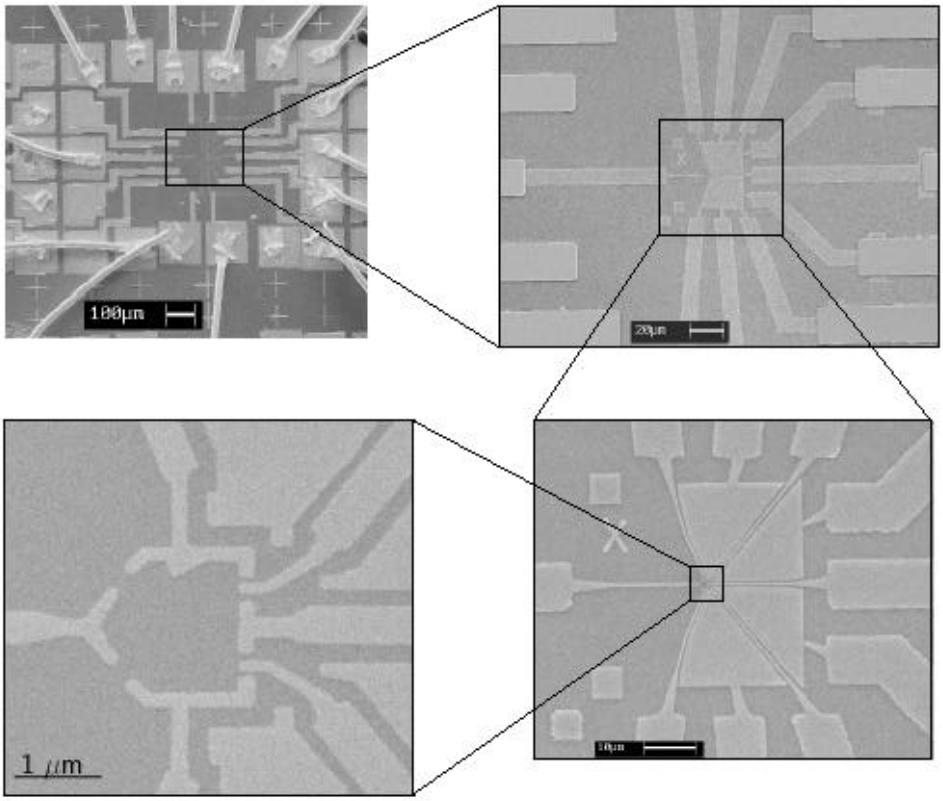

Figure A-1. SEM images of a quantum dot at increasing magnification. The upper left picture shows the ohmics and bondpads of the device with wirebonds. The other three picture show predominantly ebeam defined gates. (Dot fabrication and images courtesy of M. Switkes).

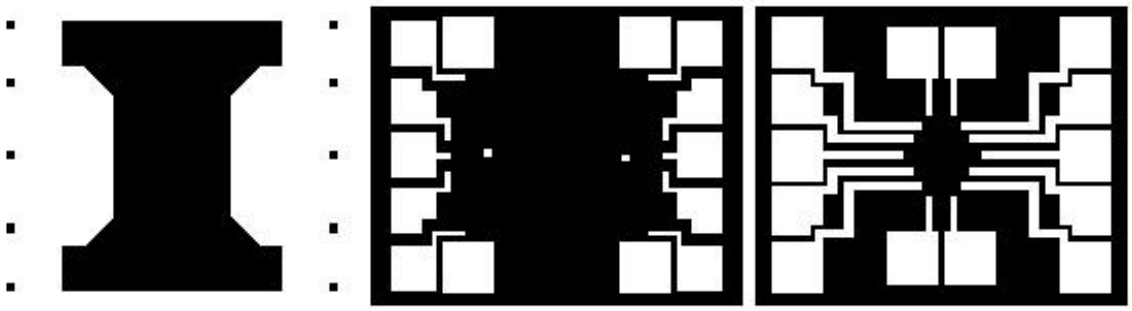

Figure A-2. Mesa, ohmic and bondpad layers of a photolithography mask. This mask, designed by M. Switkes, has been used for several generations of dots and point contacts. Dark areas represent regions of the mask covered in Cr which is opaque to ultraviolet light. The photoresist gets exposed only in the white areas. From left to right the three layers are the mesa, ohmics and bondpads for a single device. Note that only the four square ohmic pads fall on the mesa and will make electrical contact to the 2DEG.

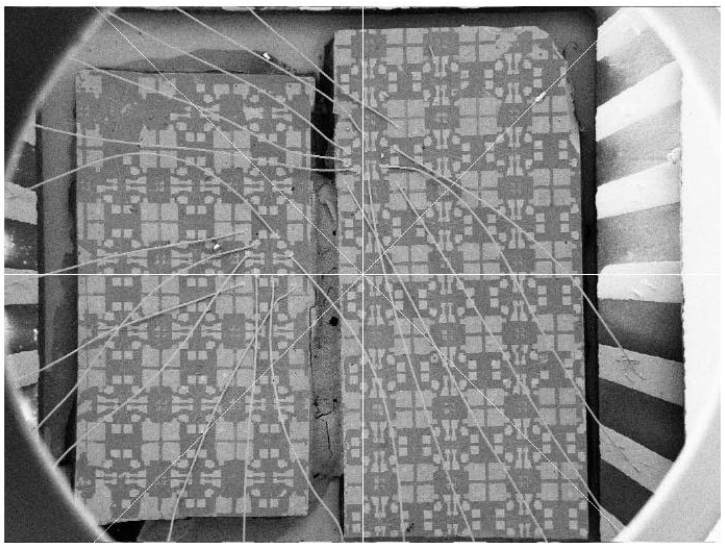

Figure A-3. SEM image of two chips in a chip carrier. The circular rim is the final aperture of the electron microscope. This chip was wire-bonded by me; one can develop an amazing ability at anything with enough practice. (Image courtesy of A. Huibers).

Appendix B

Device Noise and Testing

B.1 Background

Over the course of my thesis work, I spent a lot of time looking for “good” devices. These were devices in which the CB peak data (height and spacing) did not change over time (say on the order of 24 to 36 hours). We believe that the switching noise that we observe in most devices has to do with an impurity site near the quantum dot that can change its charge state over time. Andy Huibers shows some data of typical switching events in a quantum dot in his thesis. After doing a lot of testing, we came up with a procedure to be followed during the cool down and testing which we thought would help minimize the noise during measurement. The biggest factor in device noise is the 2DEG. After fabricating over 200+ dots on many different 2DEGs and testing around 10% of them, I am lead to believe that if the 2DEG itself is “quiet” then the chances of finding a “quiet” dot on the chips fabricated from the 2DEG are very high. Of all the 2DEGs used during my work, the most quite devices were fabricated from wafer CEM2385A from the Harris group at Stanford.

B.2 Reducing Switching Noise

Apart from the 2DEG used to fabricate the device, we found that the following items (in order) would help reduce switching noise observed during measurements:

1. Slow cool from room temperature to 4K. Although we did not do exhaustive testing to show the effectiveness of this process, we have seen good correlation between low frequency of switching events and a slow cool to 4K (over ~ 24 hours). The cooling rate is controlled by introducing a very small amount of the heat exchange gas into the IVC during the cool down step.
2. Positive gate bias during cooling. This process was suggested to us by a visiting student: David Sprinzak from Heiblum's group at Weizmann Institute of Science in Israel. The procedure involves applying ~ +0.5 V to the gates used to form the quantum dot; after cool down, a negative bias would be applied to the gates to form the quantum dot. This was not tested completely, but we always saw low switching noise after following this procedure.
3. Fridge cold time. We did observe a reduction in the low frequency switching noise (< 1 Hz) after the device had been cold for long periods of time (~ 3 – 4 weeks). This encouraged us to schedule experiments back-to-back so that a particular chip in the fridge could be kept at base temperature for as long as possible. For the same reason, we would deplete the 2DEG and form the quantum dots to be tested later even if a particular device was to be tested 1st.

Gate ramping exercise. For the long strings of CB peak data I gathered, I found that ramping the voltage on the gate over the range of interest many times (~ 50 – 100) before starting the data acquisition would lead to fewer switching events. I suspected that higher temperatures were better during this procedure and would do the exercise at 800 mK.

B.3 Testing Details

Device measurement and hardware set-up has already been covered in theses from former group members. I refer the reader to theses by: S. Cronenwett[58], A. Huibers[33], D. Stewart[21], and M. Switkes[59] for additional information.

Appendix C

AC + DC circuit Diagram

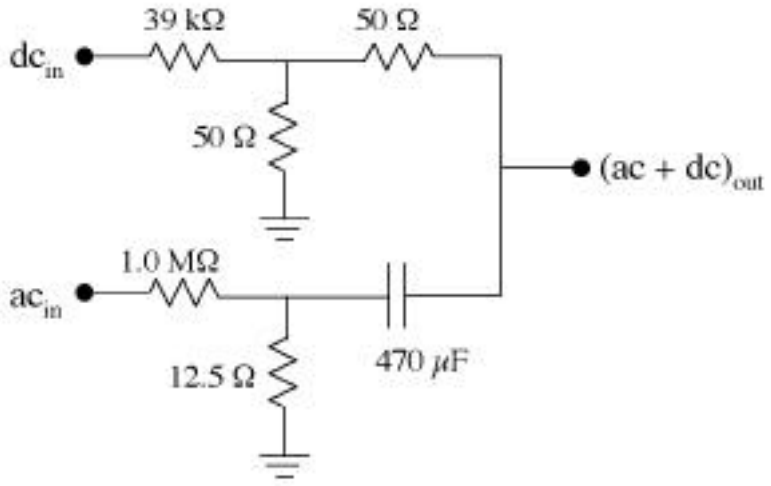

Figure C-1. Circuit used to passively add a small ac lock-in bias signal to a large dc source-drain bias. Optimized for 13 Hz; at that frequency, the dc (ac) voltage divider has 1,000:1 (10^5:1) ratio. (Figure courtesy of S. Cronenwett).

Bibliography

1. Averin, D.V. and K.K. Likharev, in *Mesoscopic Phenomena in Solids*, B.L. Altshuler, P.A. Lee, and R.A. Webb, Editors. 1991, North-Holland: Amsterdam.
2. Beenakker, C.W.J., *Theory of Coulomb-Blockade Oscillations in the Conductance of a Quantum Dot.* Physical Review B, 1991. **44**(4): p. 1646.
3. Marcus, C.M., et al., *Phase Breaking in Ballistic Quantum Dots - Experiment and Analysis Based on Chaotic Scattering.* Physical Review B, 1993. **48**(4): p. 2460.
4. Keller, M.W., et al., *Magnetotransport in a Chaotic Scattering Cavity with Tunable Electron-Density.* Surface Science, 1994. **305**(1-3): p. 501.
5. Berry, M.J., et al., *Weak-Localization and Conductance Fluctuations in a Chaotic Quantum-Dot.* Surface Science, 1994. **305**(1-3): p. 495.
6. Bird, J.P., et al., *Spectral Characteristics of Conductance Fluctuations in Ballistic Quantum Dots.* Physical Review B, 1994. **50**(24): p. 18678.
7. Huibers, A.G., et al., *Distributions of the conductance and its parametric derivatives in quantum dotsf.* Physical Review Letters, 1998. **81**: p. 200.
8. Folk, J.A., et al., *Spin degeneracy and conductance fluctuations in open quantum dots.* Physical Review Letters, 2001. **86**: p. 2102.
9. Altshuler, B.L. and B.I. Shklovskii, *Repulsion of energy levels and conductivity of small metal samples.* Soviet Physics JETP, 1986. **64**: p. 127.
10. Jalabert, R.A., H.U. Baranger, and A.D. Stone, *Conductance Fluctuations in the Ballistic Regime - a Probe of Quantum Chaos.* Physical Review Letters, 1990. **65**(19): p. 2442.
11. Baranger, H.U. and P.A. Mello, *Mesoscopic Transport through Chaotic Cavities - a Random S- Matrix Theory Approach.* Physical Review Letters, 1994. **73**(1): p. 142.
12. Beenakker, C.W.J., *Universality in the Random-Matrix Theory of Quantum Transport.* Physical Review Letters, 1993. **70**(8): p. 1155.
13. Alhassid, Y., *Statistical theory of quantum dots.* Physics Reports, 2000. **72**(4): p. 895.
14. Aleiner, I.L., P.W. Brouwer, and L. Glazman, *Quantum Effects in Coulomb Blockade.* Physics Reports, 2002. **358**(5-6): p. 309.
15. Kouwenhoven, L.P., et al., *Excitation spectra of circular, few-electron quantum dots.* Science, 1997. **278**(5344): p. 1788.
16. Stewart, D.R., et al., *Correlations between ground and excited state spectra of a quantum dot.* Science, 1997. **278**(5344): p. 1784.
17. Meirav, U. and E.B. Foxman, *Single-electron phenomena in semiconductors.* Semiconductor Science and Technology, 1996. **11**: p. 255.

18. Kouwenhoven, L.P., et al., *Electron Transport in Quantum Dots*, in *Mesoscopic Electron Transport*, L.L. Sohn, L.P. Kouwenhoven, and G. Schoen, Editors. 1997, Kluwer: Dordrecht.

19. Kouwenhoven, L. and P.L. McEuen, in *Nanotechnology*, G. Timp, Editor. 1998, AIP: New York. p. 471.

20. Beenakker, C.W.J. and H. van Houten, *Quantum Transport in Semiconductor Nanostructures*, in *Solid State Physics*, H. Ehrenreich and D. Turnbull, Editors. 1991, Academic Press: San Diego.

21. Stewart, D.R., *Level spectroscopy of a quantum dot*, in *Applied Physics*. 1999, Stanford University: Stanford.

22. Glazman, L.I. and R.I. Shekhter, *Coulomb oscillations of the conductance in a laterally confined heterostructure.* Journal of Physics: Condensed Matter, 1989. **1**(33): p. 5811.

23. Johnson, A.T., et al., *Zero-dimensional states and single electron charging in quantum dots.* Physical Review Letters, 1992. **69**: p. 1592.

24. Foxman, E.B., et al., *Effects of Quantum Levels on Transport through a Coulomb Island.* Physical Review B, 1993. **47**(15): p. 10020.

25. McEuen, P.L., et al., *Coulomb interactions and energy level spectrum of a small electron gas.* Physica B, 1993. **189**: p. 70.

26. Weis, J., et al., *Competing channels in single electron tunneling through a quantum dot.* Physical Review Letters, 1993. **71**: p. 4019.

27. Ralph, D.C., C.T. Black, and M. Tinkham, *Gate-voltage studies of discrete electronic states in aluminum nanoparticles.* Physical Review Letters, 1997. **78**(21): p. 4087.

28. Tarucha, S., et al., *Shell filling and spin effects in a few electron quantum dot.* Physical Review Letters, 1996. **77**(17): p. 3613.

29. Cronenwett, S.M., et al., *Mesoscopic fluctuations of elastic cotunneling in Coulomb blockaded quantum dots.* Physical Review Letters, 1997. **79**(12): p. 2312.

30. Maurer, S.M., et al., *Coulomb blockade fluctuations in strongly coupled quantum dots.* Physical Review Letters, 1999. **83**(7): p. 1403.

31. Cronenwett, S.M., et al., *Mesoscopic Coulomb blockade in one-channel quantum dots.* Physical Review Letters, 1998. **81**(26): p. 5904.

32. Foxman, E.B., *Single electron charging and quantum effects in semiconductor nanostructures*, in *Physics*. 1993, Massachusetts Institute of Technology: Cambridge.

33. Huibers, A.G., *Electron Transport and Dephasing in Semiconductor Quantum Dots*, in *Electrical Engineering*. 1999, Stanford University: Stanford.

34. van Houten, H., C.W.J. Beenakker, and A.A.M. Staring, *Coulomb-blockade oscillations in semiconductor nanostructures*, in *Single Charge Tunneling*, H. Grabert and M.H. Devoret, Editors. 1992, Plenum Press: New York.

35. Chang, A.M., et al., *Non-Gaussian distribution of Coulomb blockade peak heights in quantum dots.* Physical Review Letters, 1996. **76**(10): p. 1695.

36. Jalabert, R.A., A.D. Stone, and Y. Alhassid, *Statistical-Theory of Coulomb Blockade Oscillations - Quantum Chaos in Quantum Dots.* Physical Review Letters, 1992. **68**(23): p. 3468.

37. Prigodin, V.N., K.B. Efetov, and S. Iida, *Statistics of Conductance Fluctuations in Quantum Dots.* Physical Review Letters, 1993. **71**(8): p. 1230.

38. Alhassid, Y., M. Gokcedag, and A.D. Stone, *Conductance peak distributions in quantum dots at finite temperatures: Signatures of the charging energy.* Physical Review B, 1998. **58**: p. R 7524.

39. Alhassid, Y. and H. Attias, *Universal parametric correlations of conductance peaks in quantum dots.* Physical Review Letters, 1996. **76**(10): p. 1711.

40. Efetov, K.B., *Supersymmetry and Theory of Disordered Metals.* Advances in Physics, 1983. **32**(1): p. 53.

41. Bruus, H. and A.D. Stone, *Quantum chaos in a deformable billiard: Applications to quantum dots.* Physical Review B, 1994. **50**: p. 18275.

42. Huibers, A.G., et al., *Low-temperature saturation of the dephasing time and effects of microwave radiation on open quantum dots.* Physical Review Letters, 1999. **83**(24): p. 5090.

43. Folk, J.A., et al., *Statistics and parametric correlations of Coulomb blockade peak fluctuations in quantum dots.* Physical Review Letters, 1996. **76**(10): p. 1699.

44. Sivan, U., et al., *Mesoscopic fluctuations in the ground state energy of disordered quantum dots.* Physical Review Letters, 1996. **77**(6): p. 1123.

45. Simmel, F., T. Heinzel, and D.A. Wharam, *Statistics of conductance oscillations of a quantum dot in the Coulomb-blockade regime.* Europhysics Letters, 1997. **38**(2): p. 123.

46. Simmel, F., et al., *Statistics of the Coulomb-blockade peak spacings of a silicon quantum dot.* Physical Review B, 1999. **59**(16): p. R 10441.

47. Mehta, M.L., *Random Matrices*. 1991, Boston: Academic Press.

48. Blanter, Y.M., A.D. Mirlin, and B.A. Muzykantskii, *Fluctuations of conductance peak spacings in the Coulomb blockade regime: Role of electron-electron interaction.* Physical Review Letters, 1997. **78**(12): p. 2449.

49. Usaj, G. and H.U. Baranger, *Spin and e-e interactions in quantum dots: Leading order corrections to universality and temperature effects.* cond-mat/0203074, 2002.

50. Berkovits, R. and B.L. Altshuler, *Compressibility, capacitance, and ground-state energy fluctuations in a weakly interacting quantum dot.* Physical Review B, 1997. **55**(8): p. 5297.

51. Stopa, M., *Fluctuations in quantum dot charging energy and polarization.* Semiconductor Science and Technology, 1998. **13**(8A): p. A55.

52. Hackenbroich, G., W.D. Heiss, and H.A. Wiedenmuller, *Deformation of quantum dots in the Coulomb blockade regime.* Physical Review Letters, 1997. **79**: p. 127.

53. Baltin, R., et al., *Correlations of conductance peaks and transmission phases in deformed quantum dots.* European Physical Journal B, 1999. **10**: p. 119.

54. Patel, S.R., et al., *Universal fluctuations of Coulomb blockade peaks in quantum dots.* Superlattices and Microstructures, 1997. **21**(1): p. 43.

55. Patel, S.R., et al., *Statistics of Coulomb blockade peak spacings.* Physical Review Letters, 1998. **80**(20): p. 4522.

56. Patel, S.R., et al., *Changing the electronic spectrum of a quantum dot by adding electrons.* Physical Review Letters, 1998. **81**(26): p. 5900.

57. Folk, J.A., C.M. Marcus, and J.S. Harris, *Decoherence in nearly isolated quantum dots.* Physical Review Letters, 2001. **87**(20): p. 206802.

58. Cronenwett, S.M., *Coherence, charging, and spin effects in quantum dots and point contacts*, in *Physics*. 2001, Stanford University: Stanford.

59. Switkes, M., *Decoherence and Adiabatic Transport in Semiconductor Quantum Dots*, in *Physics*. 2000, Stanford University: Stanford.